Check for updates

ADVANCING EARTH AND SPACE SCIENCE

JGR Solid Earth

RESEARCH ARTICLE

10.1029/2020JB021154

Key Points:

- Integrated study of seismic anisotropy in metamorphic rocks from the COSC-1 borehole in the Swedish Caledonides
- Macroscale anisotropy is driven by major mineral assemblage, while modeled anisotropy dependent on microscale heterogeneity
- Results enable to derive facies-based anisotropy model from core lithology to be compared with field data

Supporting Information:

Supporting Information may be found in the online version of this article.

Correspondence to:

F. Kästner,
kaestner@gfz-potsdam.de

Citation:

Kästner, F., Pierdominici, S., Zappone, A., Morales, L. F. G., Schleicher, A. M., Wilke, F. D. H., & Berndt, C. (2021). Cross-scale seismic anisotropy analysis in metamorphic rocks from the COSC-1 borehole in the Scandinavian Caledonides. *Journal of Geophysical Research: Solid Earth*, *126*, e2020JB021154. https://doi.org/10.1029/2020JB021154

Received 9 OCT 2020
Accepted 29 MAR 2021

© 2021. The Authors.
This is an open access article under the terms of the Creative Commons Attribution License, which permits use, distribution and reproduction in any medium, provided the original work is properly cited.

Cross-Scale Seismic Anisotropy Analysis in Metamorphic Rocks From the COSC-1 Borehole in the Scandinavian Caledonides

Felix Kästner[1,2], Simona Pierdominici[1], Alba Zappone[3,4], Luiz F. G. Morales[3,5], Anja M. Schleicher[1], Franziska D. H. Wilke[1], and Christian Berndt[2]

[1]Helmholtz Centre Potsdam, GFZ German Research Centre for Geosciences, Potsdam, Germany, [2]GEOMAR Helmholtz Centre for Ocean Research Kiel, Kiel, Germany, [3]Department of Earth Sciences, ETH Zürich, Zurich, Switzerland, [4]Department of Mechanical and Process Engineering, ETH Zürich, Zurich, Switzerland, [5]Scientific Center for Optical and Electron Microscopy (ScopeM), ETH Zürich, Zurich, Switzerland

Abstract Metamorphic and deformed rocks in thrust zones show particularly high seismic anisotropy causing challenges for seismic imaging and interpretation. A good example is the Seve Nappe Complex in central Sweden, an old exhumed orogenic thrust zone that is characterized by a strong but incoherent seismic reflectivity and considerable seismic anisotropy. However, only little is known about their origin in relation to composition and structural influences on measurements at different seismic scales. Here, we present a new integrative study of cross-scale seismic anisotropy analyses combining mineralogical composition, microstructural analyses, and seismic laboratory experiments from the COSC-1 borehole, which sampled a 2.5-km-deep section of metamorphic rocks deformed in an orogenic root now preserved in the Lower Seve Nappe. While there is strong crystallographic preferred orientation in most samples in general, variations in anisotropy depend mostly on bulk mineral composition and dominant core lithology as shown by a strong correlation between these. This relationship enables to identify three distinct seismic anisotropy facies providing a continuous anisotropy profile along the borehole. Moreover, comparison of laboratory seismic measurements and electron-backscatter diffraction data reveals a strong scale dependence, which is more pronounced in the highly deformed, heterogeneous samples. This highlights the need for comprehensive cross-validation of microscale anisotropy analyses with additional lithological data when integrating seismic anisotropy over seismic scales.

1. Introduction

Seismic anisotropy is a powerful tool to investigate the continental crust at depth. In the upper crust, the anisotropy of seismic wave propagation is generally associated with layered sedimentary basins or extensively fractured regions, where in the former the anisotropy is caused by bedding (e.g., Bois et al., 1987; Meissner et al., 2006; Rabbel & Mooney, 1996), and in the latter by the alignment of fractures (e.g., Crampin, 1987; Kaneshima, 1990; Kern et al., 2008; Leary et al., 1990; Siegesmund & Vollbrecht, 1991). In the middle and the lower crust, the effect of seismic anisotropy can have multiple origins if observed at different scales (e.g., Babuska & Cara, 1991; Okaya et al., 2019; Weiss et al., 1999). These include layering in metamorphic and magmatic rocks (e.g., due to ductile deformation), alignment of melt pods (particularly in the oceanic lower crust), and shape/crystallographic preferred orientation (CPO) of mineral phases composing these rocks (Almqvist & Mainprice, 2017; Ji et al., 2015; Jones & Nur, 1982; Lloyd et al., 2009; Mainprice & Nicolas, 1989). Often it is not trivial to differentiate the role of each of those aspects in the resulting final seismic anisotropy (Almqvist & Mainprice, 2017) measured directly either in seismic surveys (e.g., Alkhalifah & Tsvankin, 1995; Gaiser, 1990) or in the laboratory (e.g., Burke & Fountain, 1990; Kern, 1990). In addition, crustal rocks generally present a complex mineral composition, and the determination of the role of individual mineral phases in the resulting anisotropy can be a very difficult task in the laboratory. As an example, the typical composition of schists comprises micas (highly anisotropic) mixed with feldspar and quartz (intermediately anisotropic) and garnet (generally isotropic). If these three phases are present in different proportions and potentially deformed in different magnitudes, the resulting seismic velocities, anisotropy, and propagation directions may have a complex pattern. In this context, texture-based anisotropy analyses (e.g., Mainprice et al., 2011; Prior et al., 1999) have been used to aid the identification of individual sources

that contribute to the overall rock properties (e.g., Almqvist et al., 2013; Barberini et al., 2007; Cholach & Schmitt, 2006; Erdman et al., 2013; Wenk et al., 2012).

There is a large number of studies of seismic properties and anisotropy in crustal rocks. Drilling of exhumed continental collision zones has proven to be a valuable tool to gain insights in the properties of high- and ultrahigh-pressure rocks originally formed at mid to lower crustal levels. A landmark project was the KTB deep drilling, which sampled a considerable section of upper crustal rocks from the Variscan orogeny indicating strong dependence of seismic anisotropy with fractures and microcracks. Within a major cataclastic shear zone, seismic velocities were found to decrease, while anisotropy increased by as much as 10% (Rabbel et al., 2004). Moreover, the analysis and quantification of seismic anisotropy using in situ seismic field data indicated the potential of seismic anisotropy as a tool for mapping crustal deformation zones, anisotropic terranes, and infer the in situ stress field (Okaya et al., 2004; Rabbel et al., 2004; Zang et al., 1996). Investigations on samples from the superdeep drilling project on the Kola peninsula put further constraints on the contribution of rock-forming minerals to bulk elastic anisotropy as well as pressure and temperature dependence of seismic velocities in high-grade gneisses of the Baltic Shield (Ivankina et al., 2005; Kern et al., 2001; Vernik et al., 1994). An extensive data based on laboratory seismic measurements and anisotropy of ultrahigh-pressure rocks from the Dabie-Sulu province are reported by Sun et al. (2012) as part of the Chinese Continental Scientific Drilling project. Various analyses have indicated a considerable effect of seismic anisotropy from deformed, metamorphic rocks of mainly eclogite facies due to preferred orientation of highly anisotropic minerals (Ji et al., 1993, 2013, 2015). Another example is the Outokumpu deep drilling project, which provided additional insights from seismic velocity measurements and CPO on strongly foliated biotite gneiss from the Fennoscandian Shield (Elbra et al., 2011; Kern et al., 2008; Wenk et al., 2012). There are also many experimental studies on outcrop samples representatives of various crustal levels, where the link between seismic laboratory measurements and rock microstructure is investigated. Just to mention a few examples, we would like to refer to the works on outcrops of middle and deep crustal rocks such as that from the Serie dei Laghi and the Ivrea-Verbano zone in NW Italy (e.g., Barberini et al., 2007; Barruol & Kern, 1996; Burlini & Fountain, 1993; Fountain, 1976). However, investigations from deep core samples have shown a great advantage over surface analogs that generally have been subjected to long-term weathering and alteration (Sun et al., 2012).

Here, we present the first integrative study of seismic anisotropy for the Caledonides in Sweden, of the exceptionally well-preserved Seve Nappe Complex (SNC), which is characterized by metamorphic rocks that were deformed in the roots of an orogenic belt, exhumed to upper crustal levels. In this study, we analyze and discuss the mineralogical and petrophysical attributes and their implications on the seismic anisotropy on selected core samples from the COSC-1 borehole that was drilled into the Lower Seve Nappe in Jämtland of the Central Scandinavian Caledonides (e.g., Gee et al., 2010; Lorenz et al., 2015a) (Figure 1). Initial investigations have shown the importance of seismic anisotropy in some of these rocks (Wenning et al., 2016), which led to improvements in the imaging and interpretation of seismic data (Simon et al., 2017, 2019). In this context, we complete the study that Wenning et al. (2016) have started and focus more closely on the nature and origin of the recognized anisotropy. In another related study, Kästner, Pierdominici, et al. (2020) have investigated the effects of microcracks in (depressurized) cored rocks on the seismic velocities using laboratory sample measurements as a calibration tool. Recent studies of Giuntoli et al. (2018, 2020) have been carried out with a focus on microstructural investigations to determine the age and evolution only of the mylonitic shear zone in order to constrain the pressure–temperature deformation path of the SNC.

We aim to complement the previous analyses by more detailed anisotropy investigations using also compositional and structural analysis along the entire section of the COSC-1 borehole involving different rock types. The objective of this paper is twofold and aims (i) to evaluate the relative effects of structure and composition on measured anisotropy and (ii) to compare micro- to macroscale measurements of anisotropy from laboratory and electron-backscatter diffraction (EBSD) data and their potential in extrapolating seismic properties to larger scales. To this end, we present EBSD analysis of seismic properties from core samples of the Lower Seve Nappe and investigate the role of intrinsic rock texture using analysis of the CPO and mineralogical compositional variations on the seismic anisotropy. One of the main targets of the COSC project is to properly interpret the regional seismic reflection surveys. To aid this objective, we present the first facies-based anisotropy profile for the COSC-1 borehole and discuss its implications for seismic

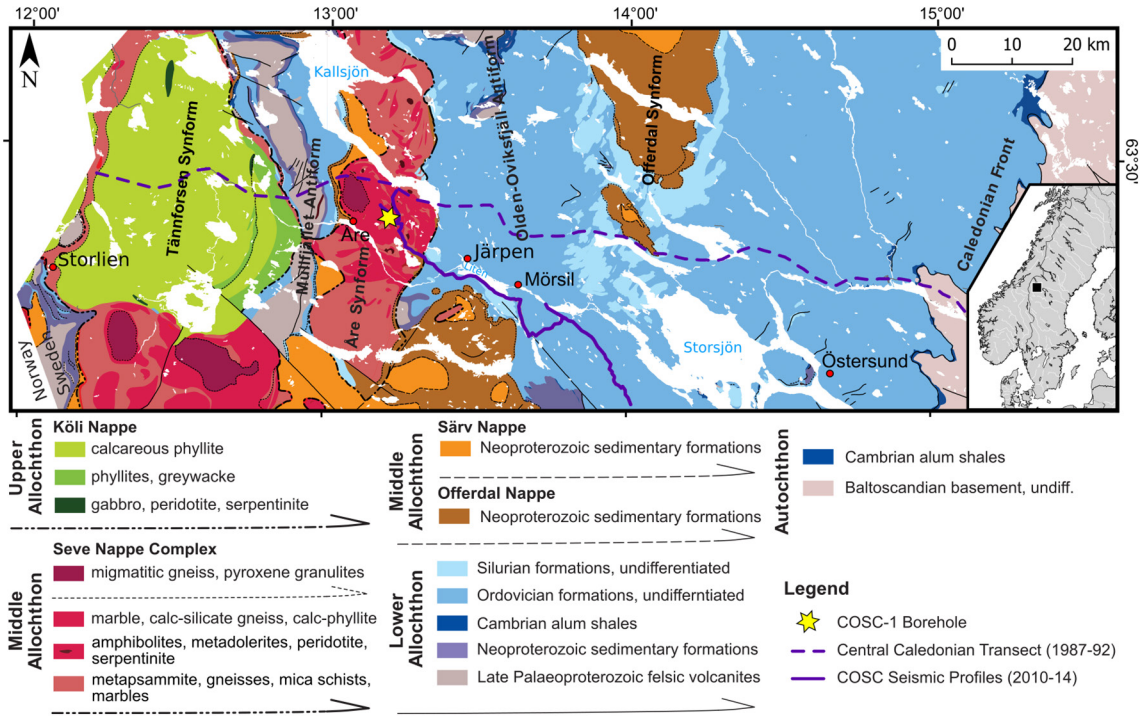

Figure 1. Geological map and tectonostratigraphy of the central Scandinavian Caledonides in Jämtland, Sweden (adapted from Hedin et al., 2016); map data from the Swedish Geological Survey (SGU) based on geological mappings from Strömberg et al. (1994).

processing. Having a suitable anisotropy profile is a fundamental step to construct an improved anisotropic velocity model.

2. Survey Location and Geological Background

The International Continental Scientific Drilling Program (ICDP) "Collisional Orogeny in the Scandinavian Caledonides (COSC)" aims to better understand the emplacement of subduction-related high-grade complexes originated at the continental margin or at the continent–ocean transition onto the Baltoscandian platform (Lorenz et al., 2015a). During the first operational phase, a borehole (COSC-1) was drilled in the vicinity of the abandoned Fröå mine, near Åre in western Jämtland, Sweden (Figure 1). The COSC-1 borehole reached a depth of almost 2.5 km and had a core recovery of nearly 100%. This core sampled a thick section of the Lower Seve Nappe and some of the underlying, lower-grade metamorphosed Särv Nappe (Lorenz et al., 2015a).

The SNC is part of a pile of thrust sheets enclosed by the adjacent Köli and (subjacent) Särv Nappes of the Middle Allochthons derived from outer Baltic margin and emplaced during the mid-Silurian continent collision and subsequent orogeny of the Scandinavian Caledonides (Gee et al., 2010; Ladenberger et al., 2014; Roberts & Gee, 1985). Internally, the SNC is characterized by an inverse metamorphic grade, reaching from upper amphibolite and eclogite facies on top toward a medium grade greenschist facies in the lower parts (Arnbom, 1980; Gee et al., 2008, 2014). The COSC-1 borehole intersects several metamorphic rock units (Figure 2) with a predominance of gneiss, mica schist, and amphibolite rocks, and an approximately 800-m-thick ductile shear zone characterized by undifferentiated mylonites encountered especially at the lower part of the borehole (Lorenz et al., 2015a). The COSC-1 borehole provides very good conditions to study seismic anisotropy on 2.5 km of exhumed middle-lower crustal rocks now preserved at upper crustal levels that are not subjected to weathering or strong retrograde metamorphism.

Core samples for the investigation of seismic properties were taken from multiple lithologies, depths, and relevant tectonic features (e.g., inferred mylonitic zone) in order to provide a sufficient representation or cross section of the drilled geology (Kästner, Pierdominici, et al., 2020; Wenning et al., 2016) (see Figure 2).

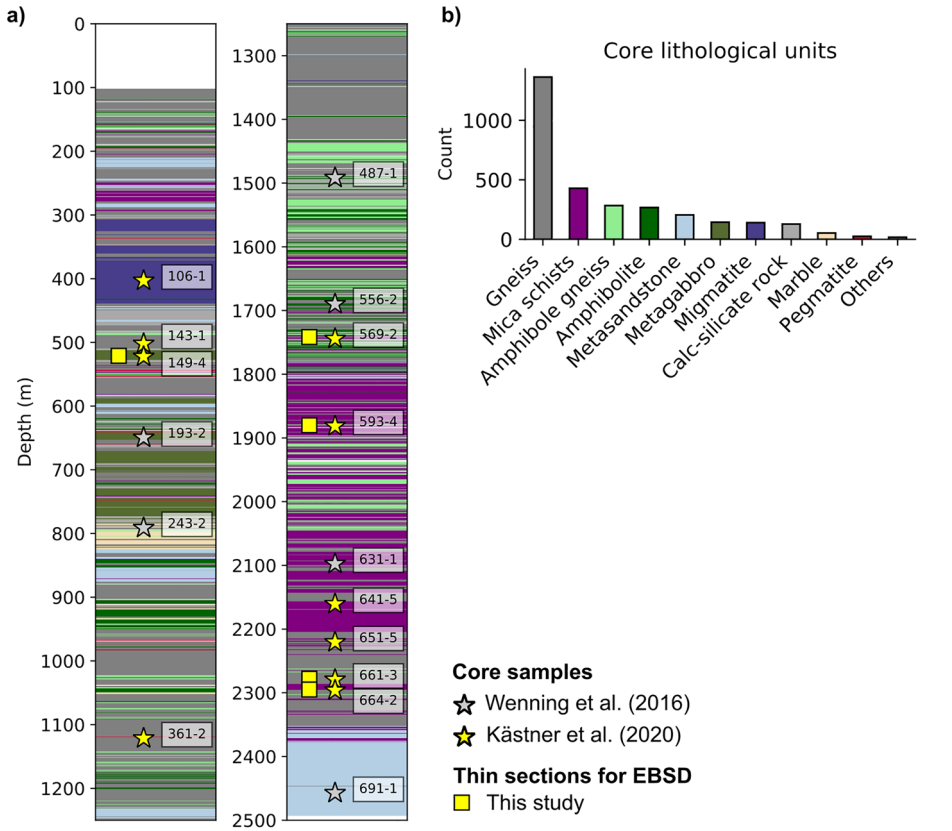

Figure 2. (a) COSC-1 core lithological profile (modified from Lorenz et al., 2015b) with locations of core samples (stars) used for laboratory seismic measurements by Kästner, Pierdominici, et al. (2020; yellow stars) and Wenning et al. (2016; gray stars). Yellow symbols indicate samples used in this study for detailed seismic anisotropy analysis using additional mineralogical analysis with XRD and electron-probe microanalyzer and complementary electron-backscatter diffraction analyses (yellow squares). (b) Distribution of the rock units based on core description in (a). XRD, X-ray powder diffractometry.

In particular, these samples were chosen from core section that are clearly represented by their core lithology. Felsic gneisses dominate the uppermost section of the borehole and can be considered as a background medium, which is frequently intertwined by mafic units, such as metagabbros and amphibolites, of changing thicknesses. While mica schists occur only sparsely in the upper section, they dominate in the deeper core sections. Within the bulk lithology, these three units are of major importance both in the reflectivity of the area and in the reconstruction of the tectonic history of the SNC (Elger et al., 2021). Moreover, the deeper-located mica schist units are presumably related to a ductile shearing zone, delimiting adjacent tectonic units.

3. Data and Methods

Based on previous studies (Kästner, Pierdominici, et al., 2020; Wenning et al., 2016), we conducted extended analysis of 10 samples for their seismic anisotropy and for their mineralogical composition and structural dependence. For the latter, we additionally chose five samples with a distinct seismic anisotropy behavior, for detailed analysis using the EBSD measurements.

3.1. Laboratory Seismic Anisotropy Measurements

A robust way to determine seismic anisotropy of a rock sample in the laboratory is to measure seismic (ultrasound) velocities from three mutually orthogonal rock plugs oriented according to the structural directions based on the visible fabric constituents (foliation and lineation). The measurements are performed

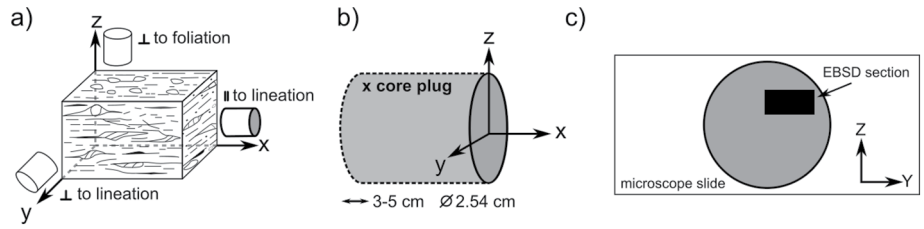

Figure 3. Sample scales and dimensions for laboratory analyses. (a) Orientation of core plugs with respect to the lineation and foliation (modified from Omura, 2004); (b) sample dimensions; (c) thin section for microscope and EBSD analysis. EBSD, electron-backscatter diffraction.

while the plugs are pressurized up to values that simulate middle crustal condition. At low confining pressure, seismic anisotropy occurs as a superposition of fracture-/crack-related anisotropy and texture-related anisotropy (e.g., Kern, 1990). With increasing pressure, microcracks and pores successively close and seismic anisotropy becomes a function of the mineral aggregate, which is also referred to as *intrinsic* seismic anisotropy (Birch, 1960).

Measurements of seismic wave velocities were conducted on 10 core samples at the Rock Physics and Mechanics Laboratory, ETH Zürich (Kästner, Pierdominici, et al., 2020). The samples cover major lithologies from a wide depth range (400–2,300 m) including both upper gneiss sections and also focus on the deeper schist units that are associated with ductile shear zones and mylonitization (Figure 2).

For the measurements, three mutually perpendicular core plugs with a diameter of 25.4 mm and length between 30 and 50 mm were drilled from each sample. The plugs were drilled accordingly to the main structural directions of the samples: x direction is parallel to lineation, y direction is perpendicular to lineation but within the foliation plane, and z direction is perpendicular to foliation (Figure 3a). These cylindrical plugs were placed between metal heads containing piezoelectric (lead–zirconate–titanite ceramic) transducers with a resonant frequency of 1 MHz. Two different types of transducers were used for compressional and shear waves. Core plug and transducers were jacketed in a polyolefin heat shrink tube before submerged in oil inside a pressure vessel. Oil pressure was increased using an air-driven fluid pump in conjunction with a compressed air system. Pressure was first increased stepwise from 50 to 250 MPa in 50 MPa, and then decreased again from 240 to 30 MPa in 30 MPa steps. At each step, the seismic waveform through the sample was recorded to determine the seismic wave arrival times. Each core plug underwent two full pressure cycles, one at increasing and one at decreasing pressure. The sample density was determined from the arithmetic mean of the densities measured on the three core plugs using a He-gas pycnometer (AccuPyc II 1340) and a precision balance. The S waves were measured according to the following polarization axes: y for the x-plug, z for the y-plug, and x for the z-plug. Thus, for the 10 samples, no shear-wave splitting (SWS) was determined. However, SWS data using two perpendicular S waves are available for six additional samples from Wenning et al. (2016). In this study, we will primarily focus on the P wave results, while, for completeness, the S wave results are provided as supporting information. See Kästner, Pierdominici, et al. (2020) for more details on the experimental setup.

Velocity–pressure curves were calculated and fitted to the measured velocity–pressure data based on a four-parameter equation, for example, proposed by Ji et al. (2007). By extrapolation of the linear high-pressure part to atmospheric pressures, we calculated the intrinsic velocity of the rock matrix excluding fabric-related elements such as microcracks induced during depressurization of the cores (Almqvist & Mainprice, 2017; Birch, 1960). Ultimately, seismic anisotropy (Av) was calculated based on the fractional difference of the minimum and maximum velocities ($v^{\max}$, $v^{\min}$) from each rock sample, following:

$$\mathrm{Av}(\%) = 100 \times \left(v^{\max} - v^{\min}\right) / v^{\max} \tag{1}$$

We derived the pressure-dependent anisotropy for each of the downgoing pressure steps. The intrinsic seismic anisotropy (Av0) is represented by linear regression of the high-pressure part and extrapolation to atmospheric pressure. By this means, any external conditions such as microfracturing are removed in order

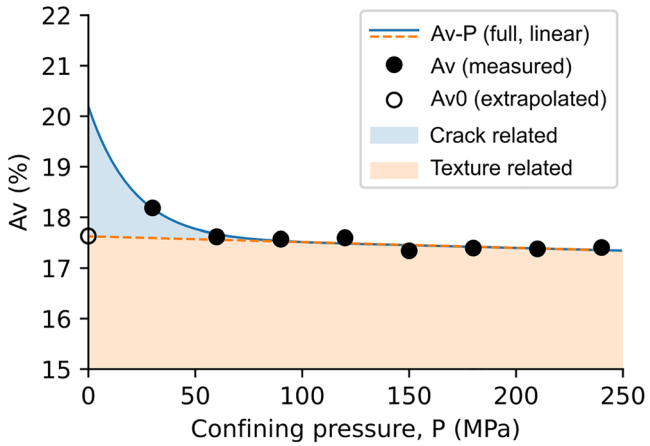

Figure 4. Example of the measured seismic velocity anisotropy as a function of confining pressure. The intrinsic anisotropy was determined from linear extrapolation of the texture-related part to atmospheric conditions. The crack- and texture-related contributions to the bulk anisotropy are highlighted.

to making the results comparable with the microscopic analysis using EBSD data from thin sections. Figure 4 exemplarily shows the anisotropy–pressure curve for sample 569-2 (mica schist) and the intrinsic anisotropy (Av0) calculated from the linear high-pressure part extrapolated to 0 MPa confining pressure.

The seismic laboratory measurements were performed at room temperature (~22°C). This agrees with the in situ (downhole) temperature conditions characterized by a low geothermal gradient (ca., 20°C/km) and generally low temperatures (<60°C) at total borehole depth (Lorenz et al., 2015b).

The uncertainty in the measured anisotropy lies below 1% for all sample measurements owing to a very high pick accuracy and high-resolution waveform data (Kästner, Pierdominici, et al., 2020). However, additional uncertainties may result from imperfect orientation of the samples with respect to their structural frame, that is, where the foliation and lineation are not as pronounced or the sample is effected by strong deformation.

3.2. Mineralogical Analysis

Mineralogical analyses were performed using optical- and electron-based microscopy (scanning electron microscope and microprobe) and X-ray powder diffractometry (XRD). We have prepared thin sections for each of the studied samples from the caps of the x core plugs, representing a slice in the sample's *y*–*z* plane, perpendicular to the foliation and lineation (Figures 3b and 3c). These thin sections were first examined under the optical microscope to get an overview of the mineral assemblage and rock fabric. After the initial optical characterization, we selected samples for electron-probe microanalysis (EPMA) to characterize the sample mineralogy quantitatively. EPMA analyses were performed using a JEOL Superprobe JXA-8230 with a LaB_6-cathode with an acceleration voltage of 15 kV, at 20 nA. The thin sections were polished with diamond solutions down to 0.25 μm grain size and carbon coated before the analysis. Compositional electron-backscatter (BSE) images of representative areas were taken using the smallest possible magnification (40X). Semiquantitative major element analyses were performed using energy dispersive spectrometry (EDX) prior to quantitative wavelength dispersive spectrometry. Quantitative analyses were prepared by calibration of Si, Al, K, Na, Ca, Mg, Ti, Fe, Mn, Ba, Cr, Cl, and F using natural and artificial silicate and oxide minerals. Feldspar, phyllosilicates, and amphiboles were measured with a defocused probe size to prevent element migration and mineral destruction.

The EPMA analyses were complemented with XRD to determine the general mineral composition of the rock samples. Therefore, the sample material was ground with a jaw crusher and subsequently sieved to a grain size of <62 μm. For quantitative mineral analysis, the powder was additionally micronized to a homogeneous powder (<10 μm) using a McCrone micronization mill. In order to gain a random distribution of the powdered sample, it was loaded from the back side of the sample holder. Analyses were performed with a Panalytical Empyrean XRD using a Bragg–Brentano geometry at 40 mA and 40 kV with CuKα radiation, and a PIXel3D detector at a step size of 0.013° 2θ from 4.6° to 85° 2θ and 60 s per step. The mineralogy was determined with the software *EVA* (version 11.0.0.3) developed by Bruker Corporation. Rietveld refinement for quantitative mineralogy was performed using the program *BGMN* (Bergmann et al., 1998) and the open-source software package *Profex* (Version 3.13.0; Doebelin & Kleeberg, 2015) calibrated for the used diffractometer. The error is in the range of 3 wt%.

3.3. Quantification of Crystallographic Preferred Orientations

To study the effect of CPO on the seismic anisotropy, we have performed EBSD measurements on 5 of the 10 rock samples that show extremes in seismic anisotropy and represent interesting geological features within the COSC stratigraphy.

EBSD analysis can be used to determine the orientation of individual grains according to the sample's coordinate axes. EBSD measurements were performed on colloidal-silica polished thin sections, in a Thermofischer/FEI Quanta 200 FEG scanning electron microscope operating with a Hikari EDAX/TSL EBSD camera and TEAM software at the Scientific Centre for Optical and Electron Microscopy of ETH Zürich. We have performed full thin section orientation mapping using step sizes of 20 μm, with an acceleration voltage of 20 kV, beam current of 8 nA, and a working distance between 17 and 20 mm. To avoid charging, samples were coated with 3 nm of carbon. Postacquisition processing included the standardization of the confidence index (CI) using a minimum grain tolerance angle of 10° and minimum 10 indexed pixels per grain, followed by a CI correlation between neighbor points, where pixels with low CI (<0.1) are reassigned to the orientation and the CI of the neighbor data point with highest CI in the individual grains. The scale relation of the analyzed sample area to the laboratory seismic measurements is shown in Figure 3.

Seismic calculations were performed using the *MTEX* toolbox for Matlab (Hielscher & Schaeben, 2008; Mainprice et al., 2011). We have used the full EBSD data sets and the elastic constants of quartz reported in Babuska and Cara (1991, p. 48), similar to the traditional one by Mcskimin et al. (1965); muscovite from Vaughan and Guggenheim (1986) plagioclase (albite, oligoclase, labradorite) reported in Brown et al. (2016); K-feldspar (orthoclase) from Waeselmann et al. (2016); and amphibole from Brown and Abramson (2016, pargasitic hornblende according to sample number 6).

The elastic constants for the aggregates were calculated using the Voigt–Reuss–Hill averaging (VRH or just Hill average) scheme (Hill, 1952; Mainprice et al., 2011), where

$$C^{\text{Voigt}} = \left[\sum_i V_i C\left(g_i\right)\right] \tag{2}$$

$$C^{\text{Reuss}} = \left[\sum_i V_i S\left(g_i\right)\right]^{-1} \tag{3}$$

and

$$C^{\text{VRH}} = 0.5 \times \left(C^{\text{Voigt}} + C^{\text{Reuss}}\right) \tag{4}$$

In these equations, $C(g_i)$ and $S(g_i)$ are the local stiffness and compliance tensors, respectively, where g is the orientation given as a triplet of Euler angles following the definition of Bunge (1982) with $g_i = \{\varphi_1, \Phi, \varphi_2\}$. While the Hill average has no physical justification it shows good results for the experimental data, especially in highly anisotropic minerals and in crystalline environments (Mainprice & Humbert, 1994). Moreover, it is also frequently applied in studies of elastic properties and, according to Almqvist and Mainprice (2017), provides a good prediction of the elastic constants (or seismic velocities) of a crystalline rock based on the modal mineral composition. An extensive and quantitative study on the effect of different mixture laws is given for example by Ji et al. (2003). We have tested our calculations with Voigt, Hill, and Reuss averages, which provide very similar results with only minor differences (generally below 1%) in our investigated rock types.

In addition to the orientation mapping, the samples were analyzed by an EDX-based phase identification yielding a 2D phase map of the investigated sample section. Giving the individual phase orientations and elastic constants, we calculated seismic velocity pole figures for each phase and the whole aggregate. Seismic anisotropy was then calculated from the maximum and minimum velocities of these poles (Mainprice et al., 2011), according to Equation 1.

4. Results

4.1. Mineralogical Composition

Based on EPMA and XRD analysis, we refine the mineralogical composition and we delineate the main structure of each core sample. Migmatite, felsic gneiss, amphibolite, mica schist, amphibole-rich gneiss, and metasandstone can be distinguished.

4.1.1. Rock Sample Description

The migmatite sample (sample 106-1) shows a clear, mainly undisturbed layering of cm-wide dark restitic bands and leucocratic melts. It consists of a fair amount of biotite concentrated in discontinuous bands, which are weakly oriented. The sample exhibits an overall weak foliation with macroscopic layering between biotite and quartz-feldspar-rich regions.

Similar texture has been found in the generally fine-grained and equigranular felsic gneiss samples (samples 143-1 and 361-2). They, however, show an increase in felsic minerals such as quartz and feldspar with an even less-pronounced schistosity. The rather few micas appear more shredded but weakly oriented.

The metagabbro (sample 149-4, name according to lithological core description) is characterized by a high amount of amphibole that comes in large grains (0.1–0.5 mm) surrounded by feldspars in a massive, very homogeneous rock matrix. A poorly visible foliation is the result of oriented amphibole and mica. In its general appearance, it is very similar to amphibolite samples as analyzed in Wenning et al. (2016, e.g., sample 193-2), except for being slightly brighter in color. Thus, in this study, the metagabbro (sample 149-4) can be synonymously treated as an amphibolite. However, to comply with the COSC-1 lithology, we kept the sample name according to the core description.

The mica schists (samples 569-2, 641-5, and 651-5) and paragneiss (sample 593-4) show a well-developed schistosity, with relatively high abundancies of mica with few intercalated, fine-grained quartz–feldspar ribbons (~0.1–0.2-mm thick). Most of the mica-rich layers (biotite and muscovite) show a strong orientation, with the development of s-c foliation. Chlorite and carbonates are minor phases and occur preferentially concentrated along bands.

Sample 661-3 is an amphibole-rich gneiss that shows the interleaving between mafic (amphibole-rich) and felsic (quartz–calcite–chlorite) bands. While the felsic bands show neither foliation nor lineation, the mafic layer is strongly foliated. Additional porphyroblasts of plagioclase show internal foliation, which is sometimes banded, likely from preexisting deformation phase.

The metasandstone (sample 664-2) shows an equigranular, homogeneous fine-grained quartz–feldspar matrix with only subordinate, weakly oriented mica.

In almost all samples except in samples 149-4 and 664-2, the foliation was clearly identified. In sample 149-4 (metagabbro) and 664-2 (metasandstone), the lineation was more difficult to determine macroscopically due to only few linear (prismatic) minerals.

4.1.2. Bulk Rock Mineralogy

All samples analyzed by XRD are primarily composed of quartz, feldspar, mica, and amphibole in different relative abundancies (Table 1). Feldspar (26% on average) can be found in all samples, with plagioclase being the major contributor. K-feldspars were found in only three samples, the felsic gneisses (samples 143-1, 361-2) and migmatite (sample 106-1). Mica can also be found in almost all samples but occur only in the mica schist and migmatite samples in considerable abundancies (>20%). Among the detected phyllosilicates, muscovite represents the dominating phase followed by biotite. Only subordinate amounts of chlorite were found in all samples, except sample 661-3. Of the more mafic minerals, we found high amounts of amphibolite (56% and 25%) in the metagabbro (sample 149-4) and amphibole-rich gneiss (sample 661-3). Pyroxene was detected in minor amounts of 5% in only four samples, migmatite (sample 106-1), felsic gneisses (samples 143-1, 361-2), and metagabbro (sample 149-4).

Within the mica schist samples, quartz can occur in various amounts, between 2% and 25%. The felsic gneisses on the other hand are clearly characterized by a high quartz and feldspar content with only little mica in the samples. Extreme amounts of quartz (72%) occur in the metasandstone sample, which is almost exclusively composed of quartz and plagioclase.

4.1.3. Mineral Chemistry, Petrology, and Petrography

We analyzed and identified major and accessory mineral phases from 10 rock samples using the microprobe. Our analyses show that mica as a major mineral phase is compositionally and morphological variable. Mica occurs in all samples mostly as iron-rich muscovite and biotite. Among the identified amphiboles,

Table 1
Summary of XRD Results Showing the Percentage of the Mineral Phases in the Whole Rock Material (Normalized to 100%)

Sample	Depth (m)	Unit	Bulk density (g cm^{-3})	Modal composition from XRD (wt%)										EBSD
				Qtz	Pl	Kfs	Bt	Ms	Am	Px	Ep	Chl	Cb	
106-1	403.09	Migmatite	2.76	1	37	21	22	0	1	5	4	0	3	
143-1	502.10	Felsic gneiss	2.73	41	33	4	3	0	3	5	5	0	4	
149-4	522.41	Metagabbro	2.99	0	33	0	3	0	56	5	0	0	2	X
361-2	1,121.48	Felsic gneiss	2.71	27	23	20	0	0	9	6	6	0	7	
569-2	1,744.27	Mica schist	2.83	2	12	0	15	60	0	0	0	4	5	X
593-4	1,881.51	Paragneiss	2.83	31	13	0	9	36	0	0	0	6	3	X
641-5	2,160.64	Mica schist	2.81	25	11	0	9	39	1	0	2	5	3	
651-5	2,220.52	Mica schist	2.77	10	26	0	10	44	1	0	1	5	2	
661-3	2,279.31	Am-rich gneiss	2.94	34	15	0	2	0	25	0	0	11	11	X
664-2	2,296.29	Metasandstone	2.68	72	19	0	3	0	0	0	3	3	0	X

Note. Samples used for EBSD analysis are marked in the last column. Qtz, quartz; Pl, plagioclase; Kfs, K-feldspar; Bt, biotite; Ms, muscovite; Am, amphibole; Px, pyroxene; Ep, epidote; Chl, chlorite; Cb, carbonates (calcite, ankerite).

tschermakite, (Mg-) hornblende, and pargasite are the dominating phases (Figure 5). We observed rare clinopyroxene in four samples, migmatite (sample 106-1), gneiss (samples 143-1 and 361-2), and metagabbro (sample 149-4), based on the element concentration these occur as augite. Plagioclase plots between about 0% and 70% of Na, thus their composition varies from albite to labradorite. K-feldspar is orthoclase and found in three samples: migmatite (sample 106-1) and gneiss (samples 143-1, and 361-2). Garnet, present in two mica schists (samples 569-2, 641-5), is almandine with 2% spessartine component. Common accessory minerals are epidotes, zircons, titanite, apatite, and opaques (ilmenite, pyrite). Secondary minerals are calcite and chlorite, where the latter occur more common in deeper-located mica schists and amphibole-rich gneiss (e.g., samples 569-2, 661-3).

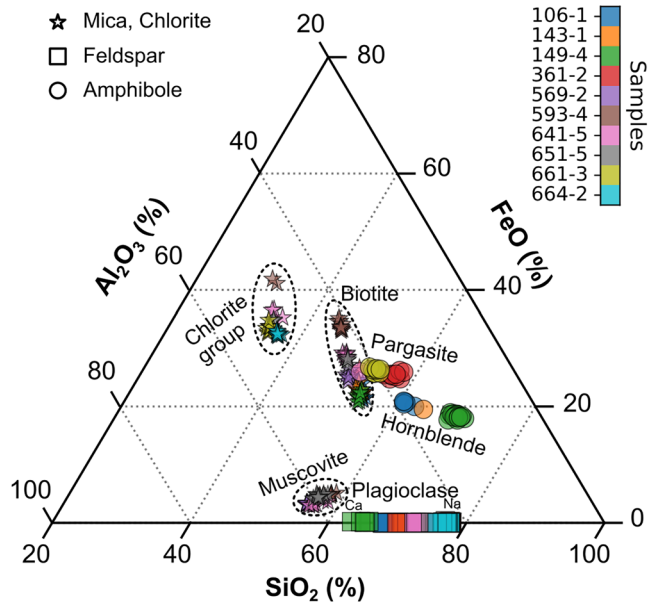

Figure 5. Sample element distribution of major mineral groups measured with the electron-probe microanalyzer. Elements are normalized to 100% of the sum of measured SiO_2, Al_2O_3, and FeO.

The mineralogy and geochemistry indicate a medium- to high-grade peak metamorphic grade for all samples, in agreement with previous studies (e.g., Giuntoli et al., 2018; Ladenberger et al., 2014).

BSE images of distinctive sample sections show a pronounced foliation caused by the alignment of muscovite and biotite. Among the mica schist (Figures 6e–6h), micas define the most pervasive foliation with evidence of tight microfolding (e.g., sample 651-5; Figure 6h). In addition, quartz and plagioclase porphyroblasts deflect the foliation planes, as we can see, for example, in mica schist (sample 569-2; Figure 6e).

Gneissic structures are well presented in samples 106-1, 143-1, and 661-3 (Figures 6a, 6c, 6d, and 6i) and are characterized by a poor-developed schistosity at microscales. Large-scale compositional layering is found, for example, in the migmatite (sample 106-1, Figure 6a). The grain size is medium to coarse with predominant anhedral crystals. Especially, the amphibole-rich gneiss (Figure 6i) shows a pronounced heterogeneous mineral assemblage, composed of chloritization of macroscopic bands of well-oriented, elongated amphiboles (predominantly pargasite) and bands of granular plagioclase, quartz, and carbonates (calcite and ankerite). Here, albite often occurs as large porphyroblasts within the amphibole-rich layers (Figure 6i). Small inclusions of Fe or Fe-Ti-oxides, carbonates, and epidote in these porphyroblasts are oriented indicating previous regional metamorphic and deformation stages.

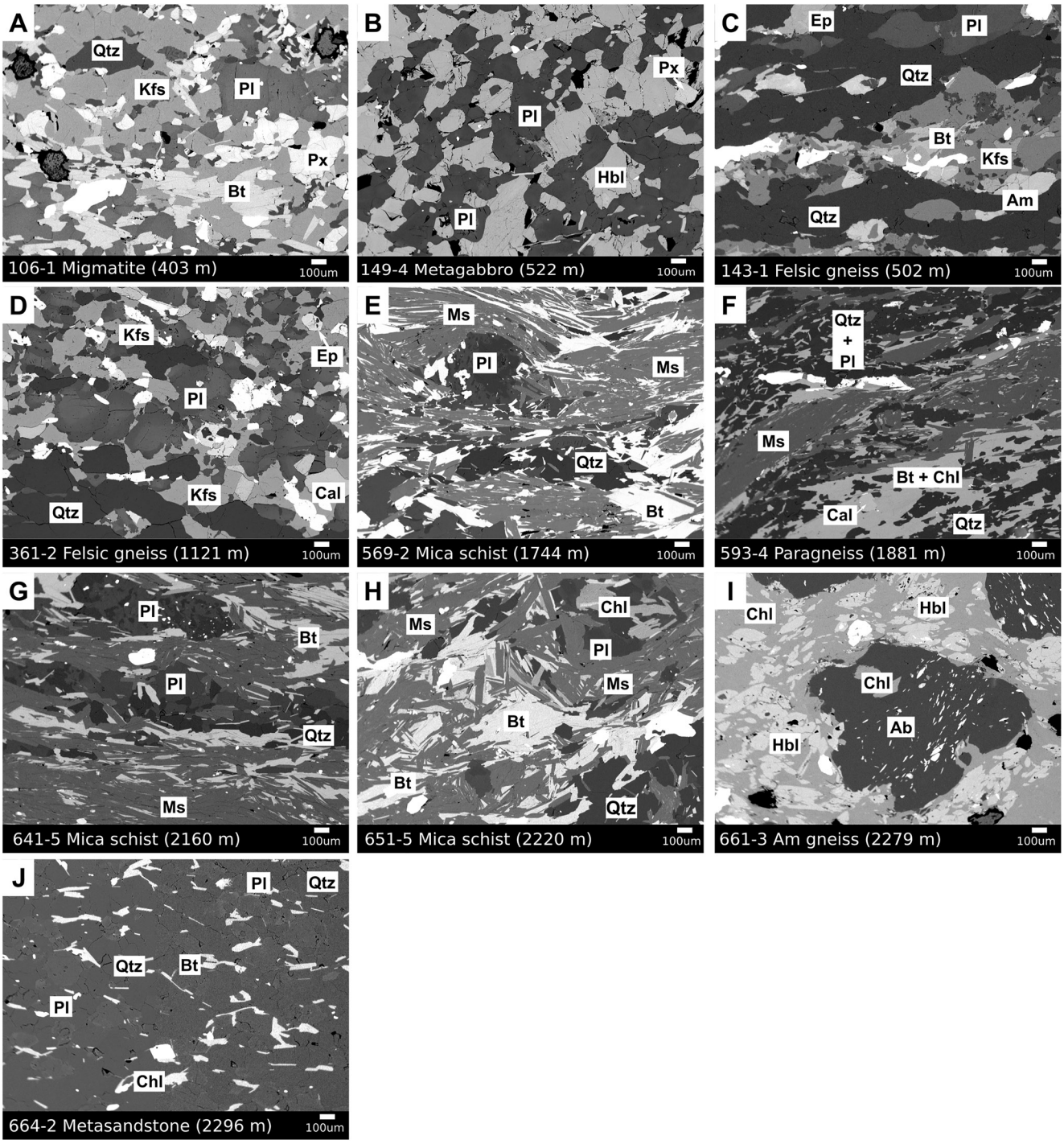

Figure 6. Back-scatter electron images of the 10 core samples. Different gray-levels for similar mineral phases between images result from different brightness and contrast adjustments and are not indicative for a different chemical composition. In most cases, if not otherwise stated, the brightest minerals refer to Fe-, Fe-Ti oxides or Ti-Si phases. Abbreviations: Ab, albite; Am, amphibole; Bt, biotite; Cal, calcite; Chl, chlorite; Ep, epidote; Hbl, hornblende; Kfs, K-feldspar; Ms, muscovite; Pl, plagioclase; Px, pyroxene; Qtz, quartz.

Metagabbro and metasandstone (samples 149-4 and 664-2, respectively; Figures 6b and 6j) show a poorly developed schistosity, having a more homogeneous, equigranular mineral distribution. The metagabbro sample (sample 149-4) contains mostly (Mg-) hornblende and labradorite whereas the metasandstone (sample 664-2) is composed of albite and quartz, as well as minor epidote and chlorite. The matrix shows no signs of recrystallization but irregular grain boundaries.

4.2. Anisotropy Investigations

4.2.1. Seismic Velocity and Anisotropy at Macroscale

Seismic *P* wave velocity and anisotropy were determined as a function of confining pressure up to 250 MPa showing distinct variations among the different samples (Figure 7 and Table S1). Linear behavior of the velocity–pressure curves was reached at about 50–70 MPa, in generally far less than 100 MPa, which indicates sufficient closure of microcracks inside all the samples at low confining pressure. The fastest velocities (at 250 MPa) were found within the *x*–*y* plane, that is, within the foliation plane of the sample. Within this plane, maximum velocities were measured along the *x* direction for samples migmatite (sample 106-1), mica schist (sample 569-2), paragneiss (sample 593-4), mica schist (samples 641-5 and 651-5), and amphibole-rich gneiss (sample 661-3). For gneiss (samples 143-1 and 361-2), metagabbro (sample 149-4), and metasandstone (sample 664-2), the fastest velocities occurred along the *y* direction. A small to moderate seismic hysteresis effect can be observed for all samples, which is generally caused by cracks and pores that remain closed after pressurization of the cores resulting in slightly higher velocities during depressurization (e.g., Ji et al., 2007).

The pressure-dependent anisotropy increases with decreasing pressure, which clearly indicates the contribution of microcracks, but only at low confining pressure. The intrinsic (i.e., crack-free) seismic anisotropy varies between 1.29% and 26.4%. Low values of seismic anisotropy (<5%) were found in migmatite, metagabbro, and metasandstone (samples 106-1, 149-4, and 664-2, respectively). Strong seismic anisotropy (>10%) is clearly observed in paragneiss (sample 593-4 with 26.4%), mica schist (samples 569-2 and 641-5 with 18%), and amphibole-rich gneiss (sample 661-3 with 14%).

While transverse isotropy ($v_P(x) \approx v_P(y) < v_P(z)$) dominates in the mica-rich samples with considerably high anisotropy (i.e., AVp > 15%), we also found indications for an orthorhombic symmetry ($v_P(x) \neq v_P(y) > v_P(z)$) in amphibole-rich gneiss and metasandstone, samples 661-3 and 664-2, respectively. In addition, the metagabbro (sample 149-4) shows a quasi-isotropic behavior, which is characterized by an extremely low anisotropy (2%) at high confining pressure (250 MPa).

For the shear waves, the anisotropy (Figure S1 and Table S1) is again very high (13%–28%) for mica schists (samples 596-2, 641-5, and 651-5) and paragneiss (sample 593-4), and intermediate to low (<10%) for the amphibole-bearing (samples 149-4 and 661-3) and gneissic samples (samples 106-1, 143-1, and 361-2). On average, the measured *S* wave anisotropy is very similar to the *P* wave anisotropy. However, in direct comparison, the *S* wave anisotropy appears to show generally higher values (2%–8%) for the mica schists (except sample 641-5) and lower values (2%–4%) for the felsic gneiss samples, compared to the *P* wave anisotropy.

4.2.2. Seismic Velocities and Anisotropy at Microscale

For the calculations of the CPO-derived seismic properties, we have averaged the elastic stiffness of the aggregate considering (1) the orientation distribution function (ODFs) of the individual phases, (2) its modal proportions, (3) the single-crystal elastic constants, and (4) their densities. The ODFs were calculated using the de la Valleé-Poussin kernel (e.g., Schaeben, 1997) assuming a constant halfwidth of 10° for all the phases. We have calculated ODFs, single and mean elastic constants, and associated velocity pole figures of five of the investigated samples for detailed analysis of the seismic velocity and anisotropy of the single mineral contributions and effect of preferred orientation (Figure 8 and Table 2). The individual ODF pole figures of the dominant phases are provided in the supporting materials (Figure S2).

In the metagabbro (sample 149-4), the anisotropy of *P* waves is basically controlled by the amphibole, while the plagioclase leads to an overall decrease in anisotropy, which results in an average anisotropy about 4%. The indexed phase map indicates an alternation of amphibole-rich and quartz- and plagioclase-rich bands which defines the foliation, and which is at an angle with the section's long axis (i.e., *y* direction).

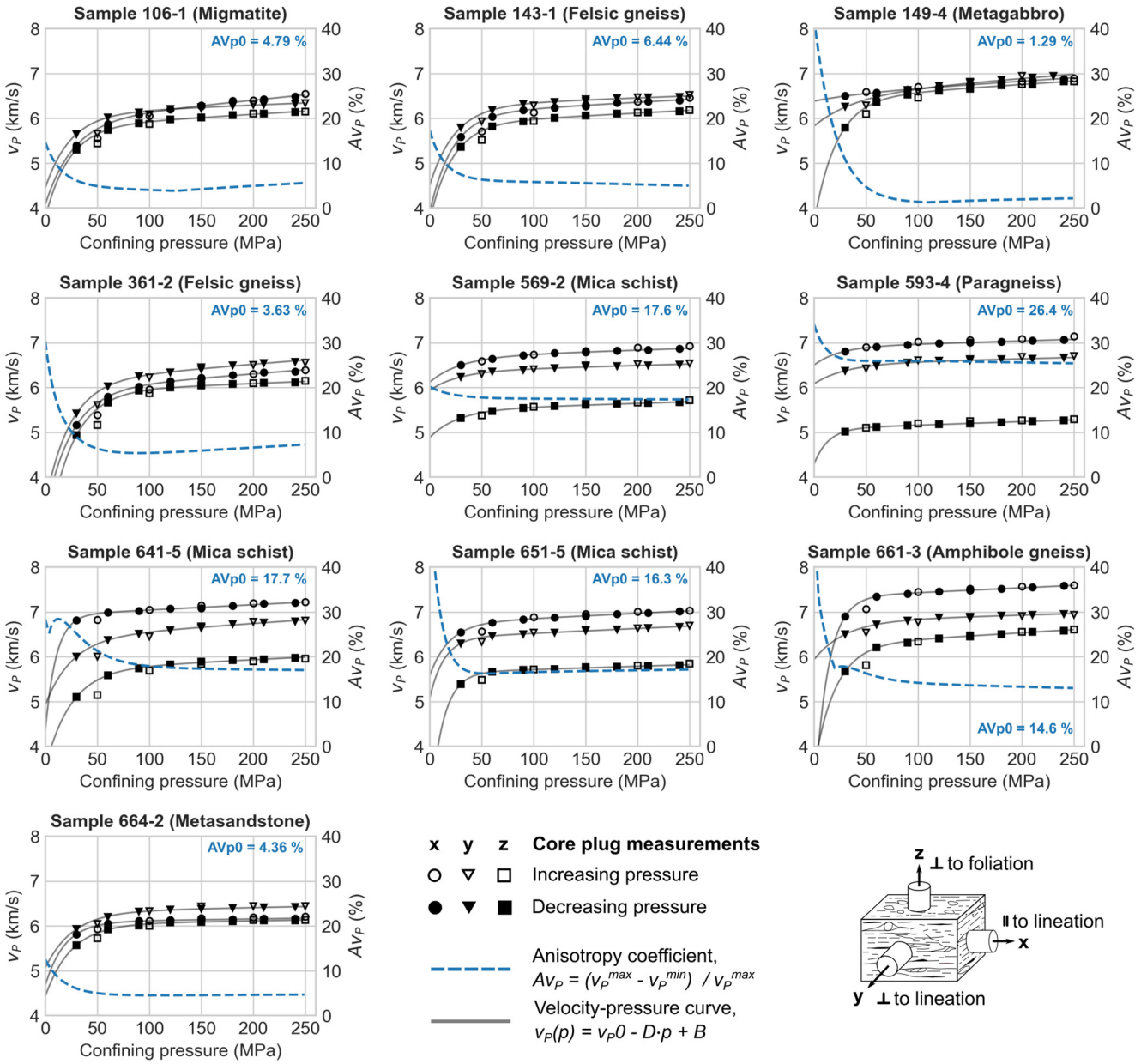

Figure 7. *P* wave velocity–pressure relation and anisotropy from laboratory seismic measurements on samples from the COSC-1 borehole. The core plug orientation (black arrows) is indicated with respect to the macroscopic fabric elements (either parallel (∥) or perpendicular (⊥) to lineation and foliation, respectively) of the sample in the lower right corner. See also Figure S1 in the supporting information for *S* wave results.

Particularly, due to the massive texture of the rock, we could not detect the foliation plane with very high accuracy and, hence, cut the cores (and consequently the thin sections) at an angle from the structural directions. This angle is nicely detected in the phase map and is visible also in the velocity pole figures of the whole aggregate. The pole figure of the aggregate indicates a weak orthorhombic symmetry, clearly derived from the symmetry of the present amphibole phase.

The mica schist (sample 569-2) is dominated by mica (muscovite) providing a strong CPO and anisotropy (24% of muscovite) in the foliation plane of the sample. Plagioclase (here oligoclase) show no strong CPO and does not contribute to the seismic anisotropy. Instead, quartz shows a relatively high CPO with its crystallographic *C*-axis (corresponding to (0001) direction) pointing in the sample's *y* direction. However, because quartz has a lower single-crystal anisotropy than mica and its maximum velocity direction is not

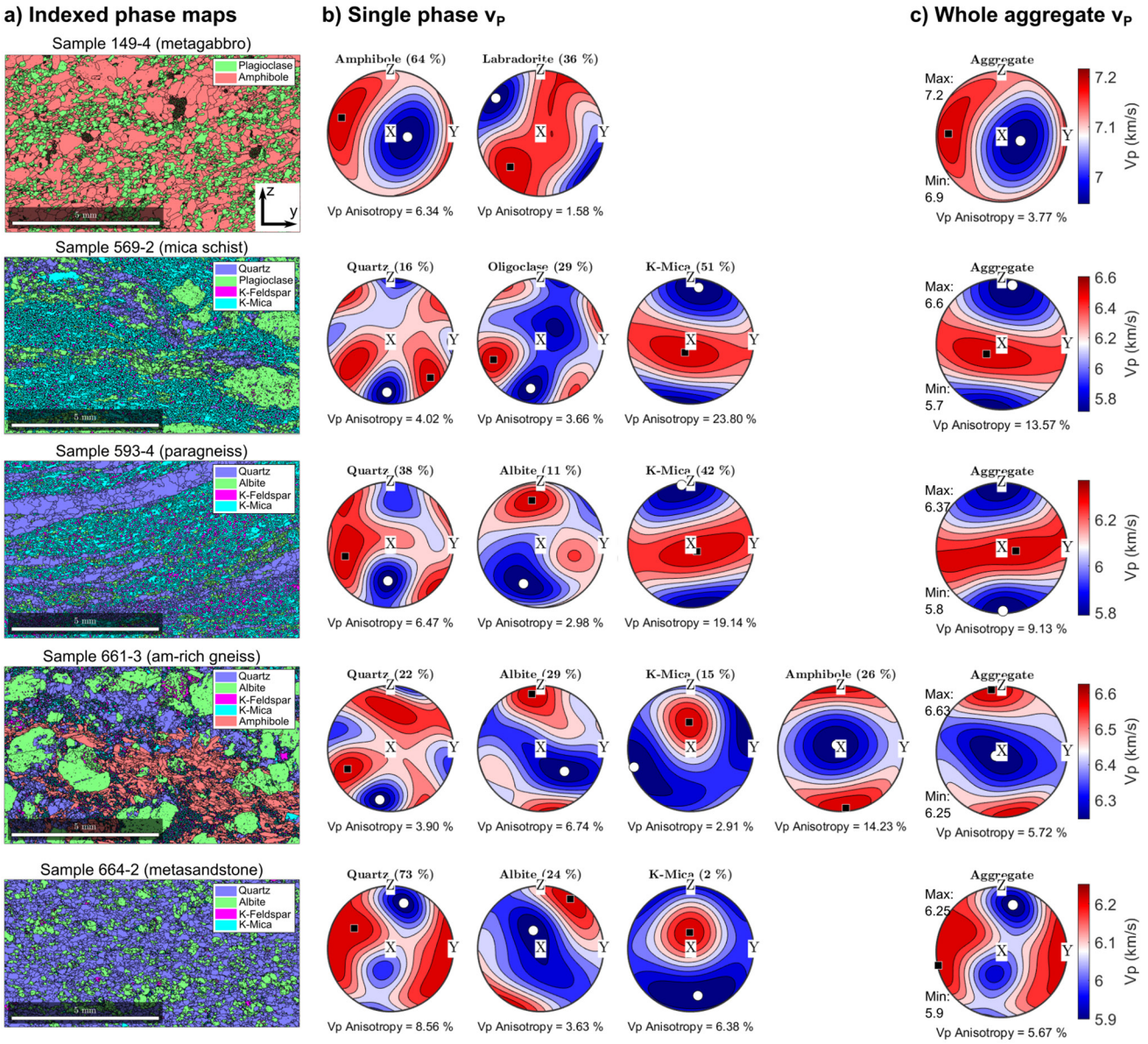

Figure 8. *P* wave velocity pole figures and anisotropy calculated for the major mineral phases and aggregates using EBSD data of five samples from the COSC-1 borehole. (a) Indexed phase maps showing the individually color-coded mineral phases and grain outlines of the EBSD section. (b) Velocity pole figures of the major mineral phases (relative abundance in percent) indicating the minimum (white circle) and maximum (black square) *P* wave velocity and resulting anisotropy according to Equation 1. (c) Velocity pole figure of the aggregate using calculated Hill average of the individual mineral phases presented in (b). EBSD, electron-backscatter diffraction.

aligned with the *C*-axis, the anisotropy of the aggregate is lowered by destructive interference to about 14%. The seismic anisotropy exhibits a clear transverse isotropic character inherited from the dominated and well-oriented muscovite.

The calculated seismic anisotropy (about 9%) of the paragneiss (sample 593-4) is dictated by the mica (muscovite), which defines, together with its strong CPO, the sample's foliation plane. The anisotropy of the constituent mica (18% for muscovite), however, is lower than in the mica schist. Quartz occurs almost exclusively in well-defined bands or ribbons stretched within the foliation plane of the sample, and therefore contributing in the definition of the foliation. Within these bands, quartz grains show a relatively strong

Table 2
Modeled Seismic Velocities (v_P) and Anisotropy (Av_P) From Hill Averages Based on EBSD Analysis

Sample	Mineral phase	Relative abundance (%)	Density (g cm^{-3})	v_P^{min} (km s^{-1})	v_P^{max} (km s^{-1})	Av_P (%)
149-4 Metagabbro	Amphibole	64	3.21	6.59	7.09	6.34
	Labradorite	36	2.64	6.86	6.97	1.58
	Aggregate	100	2.95	6.94	7.22	3.77
569-2 Mica schist	Oligoclase	29	2.64	6.49	6.74	3.66
	Quartz	16	2.65	5.90	6.15	4.02
	Orthoclase	4	2.55	5.97	6.52	8.45
	Muscovite	51	2.83	5.25	6.89	23.80
	Aggregate	100	2.75	5.71	6.61	13.57
593-4 Paragneiss	Albite	11	2.62	6.30	6.48	2.75
	Quartz	38	2.65	5.82	6.22	6.47
	Muscovite	42	2.83	5.40	6.67	19.14
	Orthoclase	8	2.55	6.07	6.65	8.71
	Aggregate	100	2.69	5.79	6.37	9.13
	Aggregate (isoMica)[a]	100	2.69	5.47	7.25	24.56
661-3 Amphibole-rich gneiss	Albite	29	2.62	6.19	6.64	6.74
	Quartz	22	2.65	5.90	6.14	3.89
	Orthoclase	8	2.55	6.13	6.52	5.93
	Muscovite	15	2.83	6.03	6.21	2.91
	Hornblende	26	3.21	6.72	7.84	14.23
	Aggregate	100	2.81	6.25	6.63	5.72
664-2 Metasandstone	Albite	24	2.62	6.3	6.54	3.63
	Quartz	73	2.65	5.71	6.24	8.56
	Orthoclase	1	2.56	6.09	6.51	6.41
	Muscovite	2	2.83	5.95	6.35	6.38
	Aggregate	100	2.65	5.90	6.25	5.67

[a]Aggregate with iso-oriented mica phase (see text for details).

CPO yielding a relatively high anisotropy (6.5%). The velocity pole figure suggests a transverse isotropic symmetry.

In the amphibole-rich gneiss (sample 661-3), the most abundant component, quartz (34%), occurs as disperse fine grains in the matrix, without strong optical iso-orientation, producing an ODF with no specific directions. Moreover, plagioclase (29%) occurs as dispersed grains with heterogeneous dimensions, without a strong CPO, producing a maximum velocity that is almost perpendicular to foliation. Hornblende (26%) is concentrated in planes defining the foliation and lineation. The ODF describes a strong concentration of the (100)-axis parallel to the samples x direction (lineation), which produces a maximum velocity perpendicular to foliation. Mica (15%) is dispersed in small grains in the rock and does not show any iso-orientation in the ODF. Its velocity pattern shows a weak maximum at a large angle from foliation along the lineation direction. The whole aggregate shows a velocity distribution completely dominated by the hornblende contribution, while quartz, plagioclase, and micas are effectively reducing the overall anisotropy.

The seismic properties of the metasandstone (sample 664-2) are clearly dominated by the abundance of quartz (73%) providing up to 9% (single-phase) anisotropy. The total anisotropy of the aggregate, however, is reduced by destructive interference with the plagioclase. The fairly low symmetry classes of quartz (trigonal) and albite (monocline) provide rather complex seismic velocity patterns. Here, quartz shows a fairly good iso-orientation of the ODF, and velocity maximum occurs approximately in the y direction, which

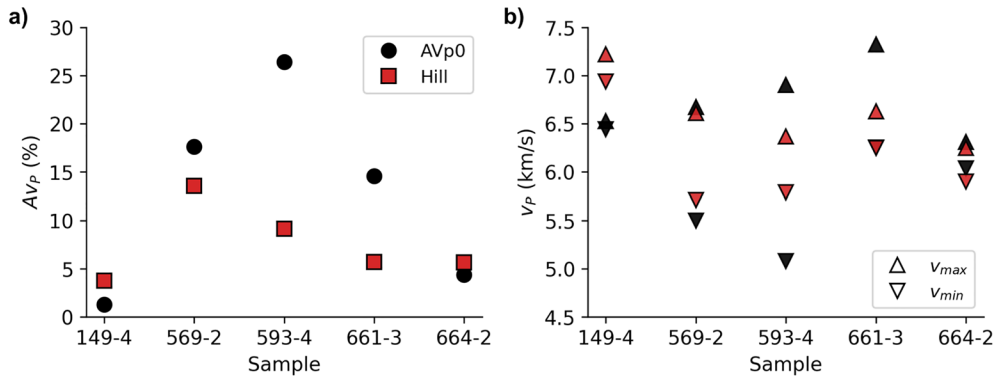

Figure 9. Comparison of *P* wave seismic anisotropy and velocities from microscale and macroscale analysis. (a) Intrinsic seismic anisotropy (at atmospheric pressure) measured on core samples (black circles) and Hill averages from EBSD microanalysis (red squares). (b) Maximum and minimum v_P velocities for selected samples determined from laboratory seismic measurements (black markers) and EBSD analysis (red markers). The laboratory data show the intrinsic seismic velocity that is the velocity of the linear high-pressure part extrapolated to atmospheric pressure. See also Tables 2 and S1, for the modeled and experimental data, respectively. EBSD, electron-backscatter diffraction.

also agrees with the laboratory measurements. Despite the very homogeneous grain distribution, a weak foliation can be recognized, which is likely determined by the mica. The symmetry of the aggregate is inherited from the rather low symmetry of the quartz phase, which, however, was modified from the original single-crystal symmetry (trigonal) due to the interference of misoriented grains.

5. Discussion

5.1. Integrated Laboratory Seismic Measurements and EBSD Analysis

In a direct comparison (Figure 9a), consistent anisotropy results between calculated Hill averages (Figure 8 and Table 2) and laboratory seismic measurements (Table S1) are mainly found for the metagabbro, mica schist, and metasandstones (samples 149-4, 569-2, and 664-2, respectively), while a significant lower anisotropy was observed, for example, in the paragneiss (sample 593-4) and amphibole gneiss (sample 593-4). In the following, we will discuss these results sample-wise in detail.

For the metagabbro (sample 149-4), we observed slightly higher seismic anisotropy calculated from the EBSD data (3.77%; Figure 8 and Table 2), compared with the experimental measurement (1.29%; Figure 7 and Table S1) showing a difference of about 2.5% (Figure 9a). This fairly small difference is expressed in a mismatch of the maximum and minimum velocities (Figure 9b), which are both higher for the modeled velocities. This can be explained by the weak foliation present in this sample. Indeed, it was difficult to identify the foliation both visually and microscopically due to the rather isotropic appearance of the sample. As a result, the three mutually perpendicular core plugs were not perfectly coaxial with the sample's structural axes, that is, its elastic extrema, leading to a reduction of the measured anisotropy. The relatively simple and homogeneous mineral composition (mainly plagioclase and amphibole) in a rather uniform matrix suggests a high confidence in the calculated EBSD result and, thus, can be used to substitute the underestimated laboratory result. Wenning et al. (2016) have shown that amphibolites from deeper (>600 m) borehole sections show a similar mineral composition. Nevertheless, their data also indicate a higher anisotropy for the amphibolites (e.g., 7.75%; sample 193-2) than for the metagabbro (3.77%; sample 149-9). We explain this by a weaker CPO, being less deformed than the deeper-located amphibolite units (Figure 2). Thus, despite their very similar mineralogy, yet their seismic properties show small variations.

The experimental and modeled seismic anisotropy of the mica schist (sample 569-2) is in relatively close agreement (17.60% and 13.57%, respectively), indicating a slight difference of 4%. This corresponds to a mismatch in the slow velocities (Figure 9b). The slightly lower anisotropy can be attributed by the slight mismatch in the abundance of plagioclase (∼30%) mapped by the EBSD compared to the bulk sample composition. Due to destructive interference, this higher amount of plagioclase effectively reduced the calculated seismic anisotropy of the aggregate. In addition, despite a pronounced foliation, the CPO of mica is not

as pervasive as expected showing many misaligned grains at microscales, also indicated by the BSE image (see Figure 6). This effectively can contribute to a reduction of the modeled anisotropy.

The paragneiss (sample 593-4) shows a significantly lower anisotropy from calculated Hill average (9.13%) than measured in the laboratory (26.41%) with a difference of ∼17%. In terms of composition, 8% K-feldspar was mapped by the EBSD, which, however, was not visible in the sample modal composition. Despite the slight variation in composition (e.g., no chlorite was mapped by the EBSD), the influence on the calculated anisotropy is comparably low and does not explain the observed difference. Calculating the Hill average with an iso-oriented mica phase (i.e., using the reference crystal orientation with the effect of CPO) suggests a significant increase in seismic anisotropy up to 20%. By additionally excluding K-feldspar, this provides a calculated seismic anisotropy of 24% (Table 2), which is close to the experimental value (26.41%). Another element that can contribute to the observed mismatch is the presence of elongated quartz ribbons, which can increase the overall anisotropy as an effect of shape-preferred orientation at core scale (e.g., Cyprych et al., 2017). However, this effect is generally minor in these rock types, especially within in a highly anisotropic mica background. Thus, an additional contribution could be given by the misorientation of the highly anisotropic minerals at the microscale. As could be shown, the degree of iso-orientation of the measured orientations of mica greatly controls the anisotropy of the whole aggregate. Thus, by means of calculating the anisotropy of the aggregate assuming only iso-oriented mica indicates a significant increase of the calculated seismic anisotropy (∼26%; see Table 2: sample 593-4, aggregate with iso-oriented mica). This value agrees well with the experimental anisotropy measured on the core plugs. This explanation is also supported by the microscope image, which indicates many grains that are not oriented in the main foliation plane. Consequently, these grains can reduce the iso-orientation of the mica and could explain the decrease in the fast velocity direction. In contrast, the experimental ultrasonic waves at the given wavelength ($\lambda = 5$–6 mm for this setup) sense predominantly the contribution from the iso-oriented mica grains. For this sample, we therefore infer an interfering effect of structural heterogeneity at microscales caused by misorientation of mica grains.

The modeled seismic anisotropy of the amphibole-rich gneiss (sample 661-3) showed very peculiar results. Here, we observed a significantly lower seismic anisotropy calculated from EBSD (5.72%) than from the laboratory seismic measurement (14.6%). Here, the disparity (∼9%) is caused by a significantly lower modeled fast velocity, whereas the slow velocities are the same for the experimental and modeled velocities (Figure 9b and Tables 2 and S1). Similar to sample 593-4 (paragneiss), we explain this disparity by the inhomogeneity of the analyzed sample area at microscale. Although the relative amounts of dominant mineral phases are comparable, the velocity pole figures of amphibole (Figure 8) provide exactly the amount of anisotropy as measured in the laboratory. This suggests that, despite a considerable amount of albite and quartz (∼50%), amphibole clearly dominates the seismic properties of the amphibole gneiss at core scales. An additional contribution from compositional banding of amphibole and mica/chlorite is here evaluated minor in contrast to the effect of the CPO of the highly anisotropic mineral phases. In particular, macrocrystals such as found in the amphibole-rich gneiss (sample 661-3) have no influence on the averaged properties at macroscales. This happens because in terms of applied sample scales the dominant wavelength of the ultrasonic measurements lies between 5 and 6 mm. The sample dimension is, thus, 10 times the dominant wavelength, which is large enough to capture all the fabric components, such as elongated quartz ribbons in the samples. In comparison, the area analyzed by the EBSD is only about twice the length of the ultrasonic wavelength. Although, this is still larger than most of the investigated grains and microstructures (like the misoriented grains in mica schist) and macrocrystals (e.g., feldspar porphyroblasts in sample 661-3) are more pronounced, thus, potentially adding to a mismatch in the mapped volume averages of the elastic constants. For a more robust analysis at microscale one, thus, can perform EBSD analysis on three perpendicular sample sections (e.g., Morales et al., 2018) and, if possible, on whole thin sections capturing more of the rock's heterogeneities.

The metasandstone (sample 664-2) showed a very homogeneous matrix that is clearly reflected in the low laboratory seismic anisotropy (4.36%), which explains its good agreement with calculated seismic anisotropy from EBSD (5.67%). The differences in the velocity extrema (Figure 9b) are within the margin of the experimental error. The velocity pole figures show that maximum and minimum *P* wave velocities (Figure 8)

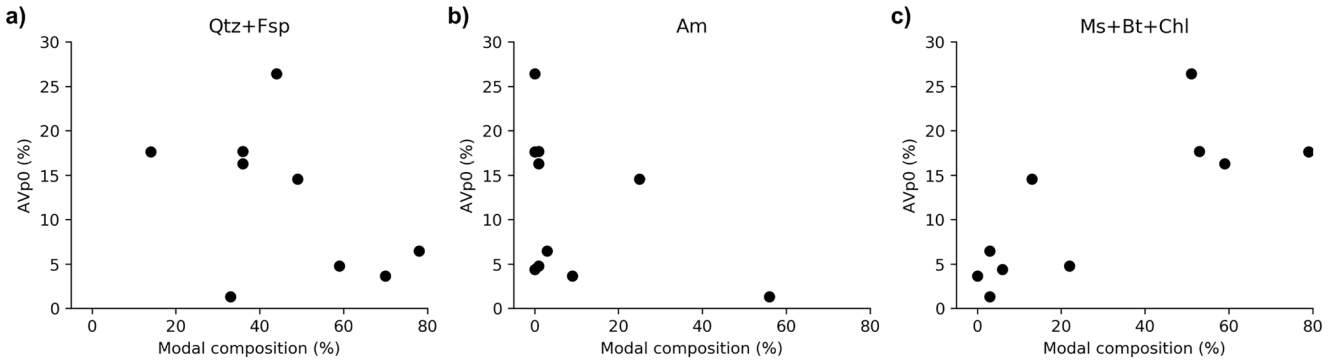

Figure 10. Intrinsic seismic anisotropy as a function of modal composition of the major minerals constituents from 10 core samples. (a) Quartz (Qtz) and feldspar (Fsp); (b) amphibole (Am); (c) muscovite (Ms), biotite (Bt), and chlorite (Chl).

do not align well with the sample's structural frame. The laboratory seismic results (Figure 7) agree well with the velocity extrema of the iso-orientated quartz as indicated by the EBSD analysis (Figure 8).

The above discussion has shown that intrinsic seismic anisotropy from laboratory seismic measurements and EBSD thin section analysis provide comparable results for homogeneous samples with uniform grain size comparable to wavelengths. Limitations are reached for more complex fabric elements, which practically are not fully covered in the microscopic analysis. As a result, in more complex cases such as in the examples of the paragneiss (sample 593-4) or the amphibole-rich gneiss (sample 661-3), sample heterogeneity at microscales is an element that has to be taken into account when using modeled data for upscaling seismic anisotropy.

Similar analyses have been conducted on core samples on ultrahigh-pressure metamorphic rocks from the Dabie-Sulu terrain in China by Sun et al. (2012). These authors list two main reasons for their observed mismatch between experimental and modeled data: (i) measured rocks may not have exactly the same chemical compositions as the single crystals for which the published elastic constants were determined; (ii) compositional heterogeneity where the thin section may not be an accurate representation of the rock sample. While both reasons can contribute to the mismatch in our samples, we evaluate the former as a minor to the second. Moreover, we found that even at microscales the effect of misoriented, highly anisotropic minerals can destructively interfere with the averaged properties which otherwise would have no effect at the macroscale measurements (scale effect). While SPO can also contribute to seismic anisotropy as for example shown for biotite gneiss from the Outokumpu deep drilling project (Wenk et al., 2012), this effect is evaluated minor in the observed difference in the modeled and measured seismic anisotropy.

5.2. Effects of Structure and Composition on Seismic Anisotropy

Different factors can control the degree of anisotropy in crystalline rocks (e.g., Babuska & Cara, 1991): (1) the anisotropy of the constituent rock minerals and their volume fraction in the aggregate; (2) the degree of crystallographic preferred orientation of minerals and fabric elements (CPO and SPO, respectively); and (3) oriented fractures and microcracks.

5.2.1. Seismic Anisotropy as a Function of Mineral Composition

To better study the seismic anisotropy as a function of mineral composition, we have grouped investigated COSC-1 samples into three major mineral units (Figure 10). Quartz–feldspar-rich rocks show rather scattered values with a high seismic anisotropy between 15% and 27% and low values less than 7% (Figure 10a). Similarly, amphibole-bearing samples show large variations of anisotropy between 0% and 26% (Figure 10b). Higher abundancies of amphibole were found only in two samples (metagabbro and amphibolite, samples 149-4 and 661-3, respectively), which show considerable differences in the seismic anisotropy (Figure 9). The last group includes mica-rich rocks (e.g., mica schist and paragneiss, samples 569-2 and 593-4, respectively) with a high amount of muscovite, biotite, and chlorite (Figure 10c). The increase of the amount of these minerals (>50% in modal composition) corresponds to an increase in anisotropy as

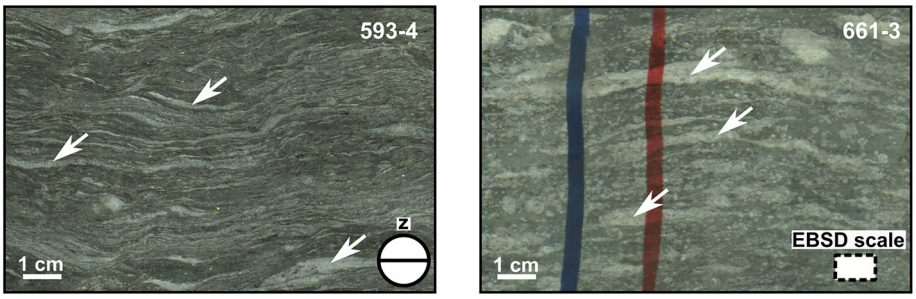

Figure 11. Section of core scan images from the COSC-1 drill core. The mylonitic fabric shows ductile deformation features such as quartz and feldspar ribbons (white arrows) at core scale. Left: paragneiss (sample 593-4). Right: amphibole-rich gneiss (sample 661-3). The sample structural frame and a scale comparison of the EBSD section are shown in the lower right corners of either image. The two colored lines in the right image indicate the core orientation as commonly marked after core extraction. EBSD, electron-backscatter diffraction.

expected due to the strong single-crystal anisotropy in connection with an overall strong CPO as indicated from the velocity pole figures (Figure 8).

We found a strong correlation of seismic anisotropy and the presence of muscovite, biotite, and chlorite in the samples, which can undoubtedly be linked to the preferred alignment of these phyllosilicates. The highest anisotropy was found in the paragneiss, which chemically resembles the mica schists. Regarding the profile of felsic (SiO_2-rich) rocks investigated in this study (Figure 2 and Table 1), the mineralogy is highly diverse, whereas the petrology seems to be more similar. According to the geochemical analysis, there is no obvious pressure or temperature gradient visible from top to bottom of the analyzed core samples (Figure 5). Thus, both the whole rock chemistry and the metamorphic grade of those rocks are responsible for the mineralogy, which behave differently under stress and strength and therefore form multiple microtextures and macrotextures and structures.

5.2.2. Seismic Anisotropy in Ductile Shear Zones

Many authors studied the effect of shear zones on the seismic rock properties (e.g., Burlini et al., 2005; Ji et al., 1997; Siegesmund et al., 1991). In ductile shear zones, mylonites can exhibit a strong anisotropy if the rock is strongly foliated and if the foliation is predominantly marked by phyllosilicates and other highly anisotropic minerals (Jones & Nur, 1982). Moreover, Kern and Wenk (1990) have shown that with increasing strain, velocity anisotropy gradually increases from a protolith to a mylonite and phyllonite. In the COSC-1 borehole, a ductile shear zone is inferred to extend almost 800 m in depth and containing several mylonites (Lorenz et al., 2015a). From the investigated samples, only the paragneiss (sample 593-4) and the amphibole-rich gneiss (sample 661-3) show signs of mylonitization (Figure 11). In addition, both samples are characterized by a higher degree of seismic anisotropy, if compared with samples of similar mineral composition. This suggests a small but contributing effect on the seismic anisotropy at macroscopic scales.

Besides a considerable effect of CPO indicated by the EBSD data (Figure 8), compositional banding can provide a potential source of seismic anisotropy in metamorphic rocks (e.g., Cyprych et al., 2017). However, this assumes a distinct separation of bands that provide significant differences in density and elastic constants such as pyroxene–garnet bands in plagioclase (Cyprych et al., 2017). Similarly, we can observe pervasive bands or ribbons of mica, plagioclase, and quartz. Most of these quartz ribbons (as found, e.g., in the paragneiss sample 593-4) occur as linear features likely formed as a result of strain elongation and dynamic recrystallization. However, they do not provide a clear compositional layering and, thus, for the investigated samples a contribution can be considered negligible.

5.2.3. Effects of Fractures and Microcracks

A considerable effect of microcracks can only be observed after full depressurization of the rocks, causing an overall reduction of seismic velocities under atmospheric pressure (Kästner, Pierdominici, et al., 2020). In addition, other studies have shown that in shallow crust regions, oriented microcracks can strongly affect the seismic anisotropy even under in situ pressure conditions as shown, for example, in rocks from the Alpine Fault (Adam et al., 2020; Simpson et al., 2020). While (micro-) cracks are present at COSC-1 borehole

depth (Wenning et al., 2017), their influence on the seismic anisotropy appears to be relatively minor to the effect of alignment of anisotropic minerals in this setting. Kästner, Pierdominici, et al. (2020) have shown that downhole sonic velocities can be approximated by intrinsic velocities for most lithologies in the COSC-1 borehole. This suggests that in the present setting microcracks become particularly important only after full core extraction and exposure to atmospheric pressure. The linearity of the velocity–pressure curves for all our samples is reached at low confining pressures showing that the effect of cracks becomes negligible above about 50–70 MPa (Figure 7). This supports the assumption of a preferably texture-related seismic anisotropy already at shallow depths for these rocks. Moreover, the linearity justifies a robust extrapolation of the crack-free anisotropy to atmospheric conditions for comparison with other measurements. Furthermore, these results could be used to robustly extrapolate the velocity and anisotropy, respectively, to higher pressure related to lower crustal zones provided of a low geothermal gradient. Besides, in our study, the effect of temperature on the seismic anisotropy was neglected, owing to very low geothermal gradient inside the COSC-1 borehole. For regions with high geothermal gradient, microcracks may reopen by thermal expansion and reverse the pressure effect (e.g., Kern, 1990). If these reopened cracks are mainly oriented, this can also contribute to the seismic anisotropy. Moreover, at very high temperatures, seismic anisotropy can also be affected by the behavior of the singly crystal properties involving phase transitions (e.g., such as in the alpha-beta transition of quartz). As an example, for a single-crystal diopside, the temperature influence in *P* wave anisotropy is minor to the pressure, whereas for *S* wave anisotropy it is vice versa (Almqvist & Mainprice, 2017, and references therein). However, for zones of low geothermal gradients and rocks with similar composition like for the COSC-1 samples, the temperature effect is almost negligible (Kern, 1978).

To summarize, our results suggest that at confining pressure above 50–70 MPa the anisotropy in the rocks of the Lower Seve Nappe is predominantly controlled by the relative abundance of the quartz/feldspars, micas, and amphiboles. At lower pressure, correlation of intrinsic velocities and borehole data also indicates that the effect of microcracks is relatively minor in most of the core lithologies. Similarly, Ji et al. (2003) could show that in the absence of fractures or microcracks the mean velocity in polymineralic rocks is predominantly controlled by the relative abundance of the constituent minerals and SPO and CPO have only minimum effects. However, an effect of SPO, although being comparably low in contrast to CPO, cannot be fully ruled out, requiring more advanced analysis. Moreover, despite a pronounced foliation observed at macroscales, the preferred orientation of the major mineral constituents was not as pervasive as expected providing the presence of microfolds, porphyroblasts, and misaligned grains can reduce the anisotropy at microscale. In addition to these findings, as discussed in the previous section, we propose that the effect of microscopic heterogeneity can lead to an underestimation of the modeled seismic anisotropy, especially for deformed metamorphic rocks with high degrees of intrinsic seismic anisotropy.

5.3. Seismic Anisotropy Across Seismic Scales

As discussed above, seismic anisotropy is a scale-variant property that can show different results based on the scale of investigation and is linked to the applied seismic wavelength (e.g., Okaya et al., 2019). In this study, we focused especially on intrinsic anisotropy based on laboratory scales involving core plugs and thin sections. Even though these measurements are strongly limited in dimension, they are valuable for seismic processing and interpretation since seismic processing relies on good velocity estimation in order to correctly place reflections at depths.

While for this study we did not observe a strong effect of compositional banding in the core samples, the COSC-1 lithological profile exhibits many zones of alternating units (Figure 2a). Especially in zones with large changes in seismic properties (such as amphibolite to gneiss/mica schist/metasandstones), this layering can lead to an additional anisotropy effect as described by the effective medium theory (Backus, 1962; Schoenberg & Muir, 1989). However, Weiss et al. (1999) have shown that this layering effect on seismic anisotropy at field seismic scales is less relevant than the actual mineral alignment. To study the effect of anisotropy even at field seismic scale, additional integration of multioffset and multiazimuth seismic experiments can be considered (e.g., Rabbel, 1994; Simon et al., 2017).

Conventional seismic anisotropy processing most commonly applies a transverse isotropic model assuming weak seismic anisotropy (<20%; Thomsen, 1986). Of our results, only the highly anisotropic mica schists are consistent with this model. Based on the approximation of an ellipsoid whose three axes correspond to

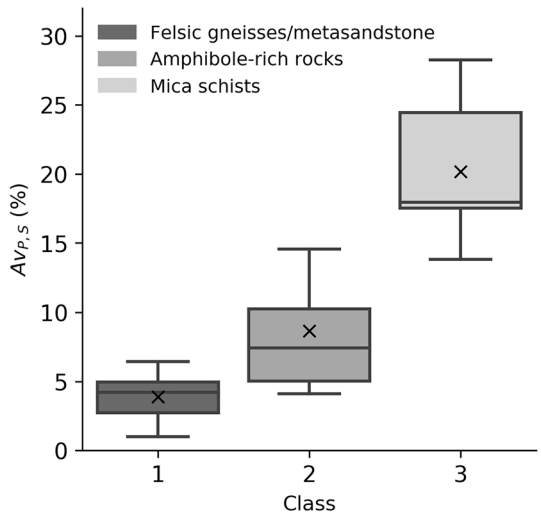

Figure 12. Anisotropy classes from seismic anisotropy measurements in metamorphic rock samples from the COSC-1 borehole (boxplots indicate mean (cross) and median (line)).

the three v_P values measured along the x, y, and z directions, the effective symmetry can also be quantified using k-values (Barberini et al., 2007) visualized in a Flinn-type diagram (see Figure S3 in the supporting information). These results suggest that the velocity surface of about 56% of the samples can be approximated by an oblate ellipsoid (i.e., being transverse isotropic), whereas 44% have a rather triaxial shape corresponding to an orthorhombic symmetry. From the calculated k-values, it becomes evident that especially the amphibole-rich samples are dominantly orthorhombic as typically expected for amphibolites. Most of the highly anisotropic mica schist are well represented by a transversely isotropic medium, whereas most of the felsic lithologies are on the transition between transverse isotropy and orthotropy (about 25% of all samples). Essentially, our results suggest an average anisotropy of at least 5% for the upper 1.7 km and about 15% on average for the lower part of the borehole section. Thus, seismic processing must account for anisotropy in order to image reflections correctly in time and space.

A first anisotropic velocity model was derived and tested by Simon et al. (2017). They used a combination of borehole-derived velocities from a vertical seismic profile (VSP) and six laboratory sample measurements providing a transverse isotropic velocity model with constant Thomsen parameters (Wenning et al., 2016). Their investigations show promising results, in particular, for the deeper seismic sections of large offset surveys. Our additional anisotropy data can aid the calibration of a near-well velocity model necessary for the short offset, limited 3D seismic survey (Hedin et al., 2016).

Based on our analysis of the sample data measured by Kästner, Pierdominici, et al. (2020) and Wenning et al. (2016), we can define three classes of anisotropy, based on their characteristic mineralogy (Figure 12): felsic gneisses-metasandstone group with the lowest $Av_P < 5\%$; the amphibolite/metagabbro/amphibole-rich gneiss group with Av_P between 6% and 13%; and the mica-rich group (including the mica schists and paragneiss) with the highest $Av_P > 17\%$. This approach clearly highlights a distinction between the different classes. The two extremes in the intermediate and high anisotropy class are due to the effect of plastic deformation causing a mylonitic microstructure as discussed above. Using these classes, we can determine an anisotropy–depth profile based on the core lithologies (Figure 13). To this end, we only considered the classified lithologies and assigned the mean anisotropy value to each unit. The same approach has been

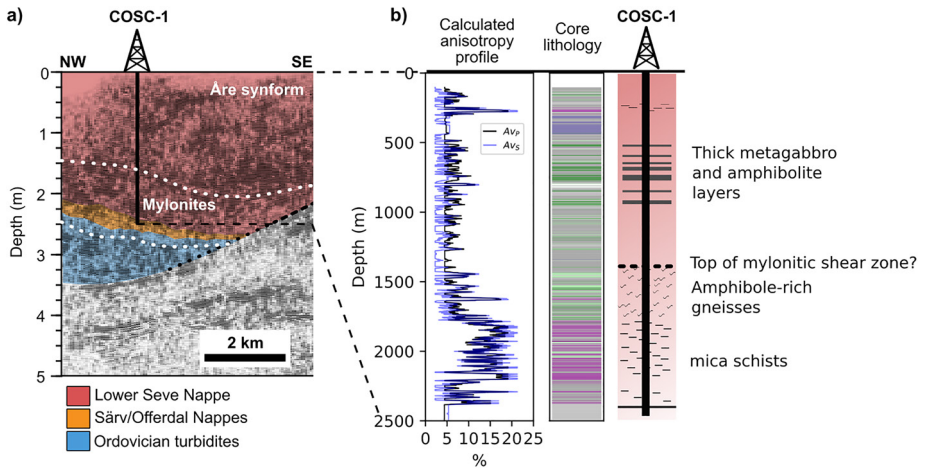

Figure 13. Anisotropy in relation to the COSC-1 stratigraphy based on simple classification approach. (a) Section of the COSC 2D seismic profile with borehole location and tectonostratigraphic interpretation (Juhlin et al., 2016). (b) Anisotropy–depth profile derived from laboratory seismic data (Kästner, Wenning, et al., 2020) and core lithology (Lorenz et al., 2015b). Simplified interpretation of the internal nappe structure is shown to the right.

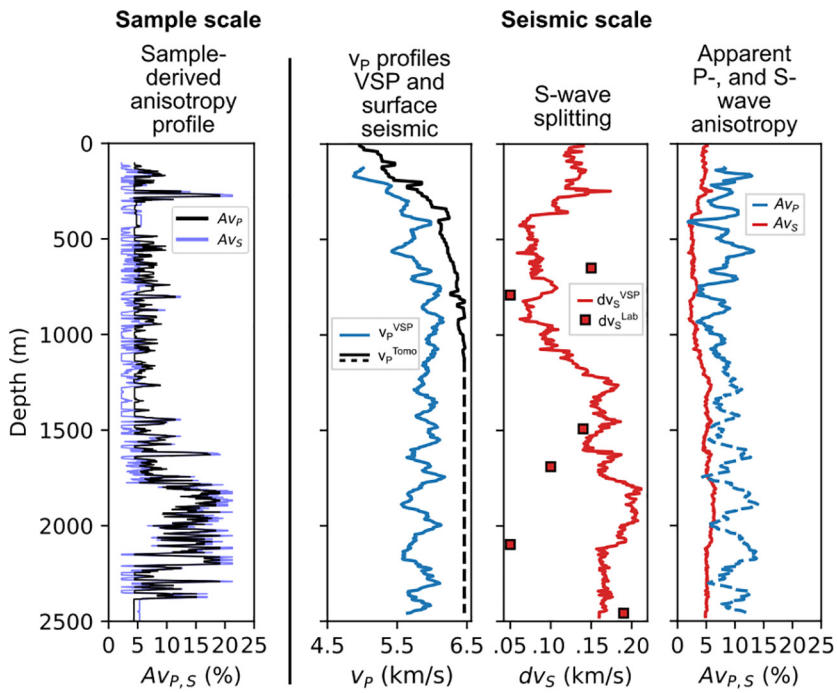

Figure 14. Sample-derived seismic anisotropy profile (first column) compared to apparent seismic anisotropy at field seismic scales (last column) derived from available and complementary borehole seismic (VSP) and surface seismic velocity profiles (column 2) based on data from Krauß (2018) and Simon et al. (2017). Column 3 shows the *S* wave splitting (SWS) from VSP (Krauß, 2018) and from seismic laboratory experiments (Wenning et al., 2016).

applied to the *S* wave anisotropy, which showed a good correlation with the *P* wave anisotropy. For visualization, the resulting profiles were smoothed with an 11-point moving average. It indicates a strong variation in seismic anisotropy along the 2.5 km section of the Åre synform with an outstanding high anisotropy below 1.6 km, which coincides with an inferred onset, yet not clearly constrained zone of highly strained mylonites in this area.

Another interesting approach to determine seismic anisotropy would be to derive it from core and downhole logs provided that both downhole sonic and core velocity logs are measured in two mutually perpendicular orientations, that is, vertical and horizontal to the borehole/core axis (e.g., Lippmann et al., 1989). Unfortunately, this does not properly work in the present setting because of a strong influence of microcracks on the depressurized core velocities obscuring the matrix rock velocity (Kästner, Pierdominici, et al., 2020).

Finally, we investigate how the macroscale anisotropy derived from laboratory samples compares to seismic velocities at seismic (regional) scales. To this end, in Figure 14, we have corendered our sample-derived seismic anisotropy profile (Figure 13b) with complementary seismic velocities based on data from combined borehole seismic (VSP) and surface seismic data at the COSC-1 borehole location (Krauß, 2018; Simon et al., 2017). The vertical velocity profile was determined directly from the first-arrival travel times of the zero-offset VSP (Krauß, 2018). The horizontal velocities were derived from a 2D first-arrival tomography, here shown directly at the COSC-1 borehole location (Simon et al., 2017). Based on these *P* wave velocity profiles, an apparent *P* wave anisotropy profile was calculated providing a rough estimate also at field seismic scales. These data suggest a strong seismic *P* wave anisotropy between 5% and 15% at depths. Because of the limited offsets, the velocity profile of the surface tomography was extrapolated from about 1.2 km downwards, providing considerable uncertainties for the deeper sections. However, these data show that considerable degrees of anisotropy can be expected at all depths, within ranges predicted by the experimental data.

Moreover, based on the data by Krauß (2018), we can approximate the seismic anisotropy from SWS analysis using a limited far-offset VSP shot survey (see Figure 14). These results also indicate a slightly higher anisotropy in the mica-rich sections of the borehole, while lower anisotropy relates to the felsic gneisses and metasandstones intervals or layers. In addition, Wenning et al. (2016) performed SWS measurements on

sample data. Their results indicated that SWS from different sample polarization is generally small (even in mica-rich rocks), providing values between 0.01 and 0.19 km/s. In comparison with those from VSP, which yield about 0.05–021 km/s, within similar ranges. In contrast, for example, Cholach et al. (2005), reported a SWS of up to 0.77 km/s for similar rock types, as a result of mesoscale fracturing. Here, we interpret the relative low SWS by a low effect of fracture anisotropy. Acoustic borehole image log analysis also confirms the absence of strong fracturing for the COSC-1 borehole (Wenning et al., 2017). Transferred into an apparent *S* wave anisotropy, the SWS profile from VSP suggests a generally lower *S* wave anisotropy, in comparison to the *P* wave anisotropy profiles predicted from the laboratory sample data and from the combined surface and borehole seismic velocity data (Figure 14). Further investigations of these data and more elaborate VSP geometries may help to improve the velocity and anisotropy models of the borehole vicinity at field seismic scales.

Our here proposed anisotropy profile depicts only a one-dimensional representation of a fairly complex and likely heterogeneous geology and, thus, its lateral extent is constrained to the borehole vicinity. Its use, however, can aid the construction of (regional) seismic velocity models important for seismic processing involving time-to-depth conversions or seismic depth migration schemes.

6. Conclusions

The seismic anisotropy investigated in metamorphic rocks of the Lower Seve Nappe is clearly expressed in the bulk core lithology, which can be represented by three distinct seismic anisotropy facies providing a continuous anisotropy profile. The seismic anisotropy facies can aid the construction of an anisotropic velocity model to better image reflection seismic data in this region.

EBSD data as standard methodology for calculating seismic anisotropy allow to extrapolate seismic properties also to macro and field seismic scales. This works well in fairly undisturbed and homogeneous microstructures such as metagabbro, amphibolite, and metasandstone, while it should be carried out in connection with laboratory seismic measurements in (mylonitic) deformed and heterogenic samples, too. In particular, microscale heterogeneities and microstructural deformation can lead to an underestimation of seismic anisotropy.

Despite pronounced CPO throughout all rock samples, we have found a strong correlation of seismic anisotropy with bulk composition and the abundance of primarily mica and second amphibole, while destructive interference was observed mainly for the quartz and feldspar phases. Velocity pole figures suggest that transverse isotropy suits best where formations are rich in mica schists, whereas for other lithologies, more complex (lower) symmetries must be taken into account.

The here presented data highlight the importance of seismic anisotropy within metamorphic rocks deformed in orogenic roots, which have been exhumed to upper crustal levels.

Acknowledgments
This research was funded by the Deutsche Forschungsgemeinschaft (DFG, German Research Foundation)—Project no. 339380967 (SPP-1006). The COSC-1 drilling project was supported by the International Continental Scientific Drilling Program (ICDP) and the Swedish Research Council (VR, grant 2013–94) using the national research infrastructure for scientific drilling *Riksriggen*. We thank Whitney Behr from ETH Zürich for funding of the EBSD measurements. We also thank Nicolai Klitscher (GFZ Potsdam) for preparation of the thin sections and Jasmin Jenichen (GFZ Potsdam) for preparation of the sample powder for XRD. We would like to thank Bjarne Almqvist (Uppsala University) and Ulrich Harms (GFZ Potsdam) for their comments and suggestions during manuscript preparation. Laboratory measurements were conducted at the Rock Physics and Mechanics Laboratory at the ETH Zürich, under supervision of Claudio Madonna. We are particularly grateful to the Associate Editor Ludmila Adam, the reviewer Wolfgang Rabbel, and one anonymous reviewer for their valuable comments and critical review that greatly improved the manuscript. Open access funding enabled and organized by Projekt DEAL.

Data Availability Statement

The data supporting the conclusion are available through the GFZ Data Services repository (https://doi.org/10.5880/GFZ.4.2.2020.009).

References

Adam, L., Frehner, M., Sauer, K., Toy, V., & Guerin-Marthe, S. (2020). Seismic anisotropy and its impact on imaging the shallow Alpine Fault: An experimental and modeling perspective. *Journal of Geophysical Research: Solid Earth*, *125*, e2019JB019029. https://doi.org/10.1029/2019JB019029

Alkhalifah, T., & Tsvankin, I. (1995). Velocity analysis for transversely isotropic media. *Geophysics*, *60*(5), 1550–1566. https://doi.org/10.1190/1.1443888

Almqvist, B. S. G., Hirt, A. M., Herwegh, M., Ebert, A., Walter, J. M., Leiss, B., & Burlini, L. (2013). Seismic anisotropy in the Morcles nappe shear zone: Implications for seismic imaging of crustal scale shear zones. *Tectonophysics*, *603*, 162–178. https://doi.org/10.1016/j.tecto.2013.05.025

Almqvist, B. S. G., & Mainprice, D. (2017). Seismic properties and anisotropy of the continental crust: Predictions based on mineral texture and rock microstructure. *Reviews of Geophysics*, *55*, 367–433. https://doi.org/10.1002/2016RG000552

Arnbom, J.-O. (1980). Metamorphism of the Seve Nappes at Åreskutan, Swedish Caledonides. *Geologiska Foreningen i Stockholm Forhandlingar*, *102*(4), 359–371. https://doi.org/10.1080/11035898009454493

Babuska, V., & Cara, M. (1991). *Seismic anisotropy in the Earth* (Vol. 10). Dordrecht, The Netherlands: Springer. https://doi.org/10.1007/978-94-011-3600-6

Backus, G. E. (1962). Long-wave elastic anisotropy produced by horizontal layering. *Journal of Geophysical Research*, *67*(11), 4427–4440. https://doi.org/10.1029/JZ067i011p04427

Barberini, V., Burlini, L., & Zappone, A. (2007). Elastic properties, fabric and seismic anisotropy of amphibolites and their contribution to the lower crust reflectivity. *Tectonophysics*, *445*(3–4), 227–244. https://doi.org/10.1016/J.TECTO.2007.08.017

Barruol, G., & Kern, H. (1996). Seismic anisotropy and shear-wave splitting in lower-crustal and upper-mantle rocks from the Ivrea zone—Experimental and calculated data. *Physics of the Earth and Planetary Interiors*, *95*(3–4 SPEC. ISS.), 175–194. https://doi.org/10.1016/0031-9201(95)03124-3

Bergmann, J., Friedel, P., & Kleeberg, R. (1998). BGMN—A new fundamental parameters based Rietveld program for laboratory X-ray sources; it's use in quantitative analysis and structure investigations. *Commission on Powder Diffraction (IUCr) Newsletter*, *20*, 5–8.

Birch, F. (1960). The velocity of compressional waves in rocks to 10 kilobars: 1. *Journal of Geophysical Research*, *65*(4), 1083–1102. https://doi.org/10.1029/JZ065i004p01083

Bois, C., Cazes, M., Hirn, A., Matte, P., Mascle, A., Montadert, L., & Pinet, B. (1987). Crustal laminations in deep seismic profiles in France and neighbouring areas. *Geophysical Journal International*, *89*(1), 297–304. https://doi.org/10.1111/j.1365-246X.1987.tb04422.x

Brown, J. M., & Abramson, E. H. (2016). Elasticity of calcium and calcium–sodium amphiboles. *Physics of the Earth and Planetary Interiors*, *261*, 161–171. https://doi.org/10.1016/j.pepi.2016.10.010

Brown, J. M., Angel, R. J., & Ross, N. L. (2016). Elasticity of plagioclase feldspars. *Journal of Geophysical Research: Solid Earth*, *121*, 663–675. https://doi.org/10.1002/2015JB012736

Bunge, H.-J. (1982). *Texture analysis in materials science*. Oxford: Butterworth-Heinemann. https://doi.org/10.1016/C2013-0-11769-2

Burke, M. M., & Fountain, D. M. (1990). Seismic properties of rocks from an exposure of extended continental crust—New laboratory measurements from the Ivrea Zone. *Tectonophysics*, *182*(1–2), 119–146. https://doi.org/10.1016/0040-1951(90)90346-A

Burlini, L., Arbaret, L., Zeilinger, G., & Burg, J.-P. (2005). High-temperature and pressure seismic properties of a lower crustal prograde shear zone from the Kohistan Arc, Pakistan. *Geological Society Special Publication*, *245*, 187–202. https://doi.org/10.1144/GSL.SP.2005.245.01.09

Burlini, L., & Fountain, D. M. (1993). Seismic anisotropy of metapelites from the Ivrea-Verbano zone and Serie dei Laghi (northern Italy). *Physics of the Earth and Planetary Interiors*, *78*(3–4), 301–317. https://doi.org/10.1016/0031-9201(93)90162-3

Cholach, P. Y., Molyneux, J. B., & Schmitt, D. R. (2005). Flin Flon Belt seismic anisotropy: Elastic symmetry, heterogeneity, and shear-wave splitting. *Canadian Journal of Earth Sciences*, *42*(4), 533–554. https://doi.org/10.1139/e04-094

Cholach, P. Y., & Schmitt, D. R. (2006). Intrinsic elasticity of a textured transversely isotropic muscovite aggregate: Comparisons to the seismic anisotropy of schists and shales. *Journal of Geophysical Research*, *111*, B09410. https://doi.org/10.1029/2005JB004158

Crampin, S. (1987). Geological and industrial implications of extensive-dilatancy anisotropy. *Nature*, *328*(6130), 491–496. https://doi.org/10.1038/328491a0

Cyprych, D., Piazolo, S., & Almqvist, B. S. G. (2017). Seismic anisotropy from compositional banding in granulites from the deep magmatic arc of Fiordland, New Zealand. *Earth and Planetary Science Letters*, *477*, 156–167. https://doi.org/10.1016/j.epsl.2017.08.017

Doebelin, N., & Kleeberg, R. (2015). Profex: A graphical user interface for the Rietveld refinement program BGMN. *Journal of Applied Crystallography*, *48*(5), 1573–1580. https://doi.org/10.1107/S1600576715014685

Elbra, T., Karlqvist, R., Lassila, I., Haeggström, E., & Pesonen, L. J. (2011). Laboratory measurements of the seismic velocities and other petrophysical properties of the Outokumpu deep drill core samples, eastern Finland. *Geophysical Journal International*, *184*(1), 405–415. https://doi.org/10.1111/j.1365-246X.2010.04845.x

Elger, J., Berndt, C., Kästner, F., Pierdominici, S., Kück, J., Almqvist, B. S. G., et al. (2021). Core-log-seismic integration in metamorphic rocks and its implication for the regional geology: A case study for the ICDP Drilling Project COSC-1, Sweden. *Geochemistry, Geophysics, Geosystems*, *22*, e2020GC009376. https://doi.org/10.1029/2020GC009376

Erdman, M. E., Hacker, B. R., Zandt, G., & Seward, G. (2013). Seismic anisotropy of the crust: Electron-backscatter diffraction measurements from the Basin and Range. *Geophysical Journal International*, *195*(2), 1211–1229. https://doi.org/10.1093/gji/ggt287

Fountain, D. M. (1976). The Ivrea-Verbano and Strona-Ceneri Zones, Northern Italy: A cross-section of the continental crust—New evidence from seismic velocities of rock samples. *Tectonophysics*, *33*(1–2), 145–165. https://doi.org/10.1016/0040-1951(76)90054-8

Gaiser, J. E. (1990). Transversely isotropic phase velocity analysis from slowness estimates. *Journal of Geophysical Research*, *95*(B7), 11241. https://doi.org/10.1029/JB095iB07p11241

Gee, D. G., Fossen, H., Henriksen, N., & Higgins, A. K. (2008). From the early Paleozoic platforms of Baltica and Laurentia to the Caledonide Orogen of Scandinavia and Greenland. *Episodes*, *31*(1), 44–51.

Gee, D. G., Juhlin, C., Pascal, C., & Robinson, P. (2010). Collisional Orogeny in the Scandinavian Caledonides (COSC). *Gff*, *132*(1), 29–44. https://doi.org/10.1080/11035891003759188

Gee, D. G., Ladenberger, A., Dahlqvist, P., Majka, J., Be'eri-Shlevin, Y., Frei, D., & Thomsen, T. (2014). The baltoscandian margin detrital zircon signatures of the central Scandes. *Geological Society, London, Special Publications*, *390*(1), 131–155. https://doi.org/10.1144/SP390.20

Giuntoli, F., Menegon, L., & Warren, C. J. (2018). Replacement reactions and deformation by dissolution and precipitation processes in amphibolites. *Journal of Metamorphic Geology*, *36*(9), 1263–1286. https://doi.org/10.1111/jmg.12445

Giuntoli, F., Menegon, L., Warren, C. J., Darling, J., & Anderson, M. (2020). Protracted shearing at mid-crustal conditions during large-scale thrusting in the Scandinavian Caledonides. *Tectonics*. https://doi.org/10.1029/2020TC006267

Hedin, P., Almqvist, B., Berthet, T., Juhlin, C., Buske, S., Simon, H., et al. (2016). 3D reflection seismic imaging at the 2.5 km deep COSC-1 scientific borehole, central Scandinavian Caledonides. *Tectonophysics*, *689*, 40–55. https://doi.org/10.1016/j.tecto.2015.12.013

Hielscher, R., & Schaeben, H. (2008). A novel pole figure inversion method: Specification of the MTEX algorithm. *Journal of Applied Crystallography*, *41*(6), 1024–1037. https://doi.org/10.1107/S0021889808030112

Hill, R. (1952). The elastic behaviour of a crystalline aggregate. *Proceedings of the Physical Society. Section A*, *65*(5), 349–354. https://doi.org/10.1088/0370-1298/65/5/307

Ivankina, T. I., Kern, H. M., & Nikitin, A. N. (2005). Directional dependence of P- and S-wave propagation and polarization in foliated rocks from the Kola superdeep well: Evidence from laboratory measurements and calculations based on TOF neutron diffraction. *Tectonophysics*, *407*(1–2), 25–42. https://doi.org/10.1016/j.tecto.2005.05.029

Ji, S., Long, C., Martignole, J., & Salisbury, M. (1997). Seismic reflectivity of a finely layered, granulite-facies ductile shear zone in the southern Grenville Province (Quebec). *Tectonophysics*, *279*(1–4), 113–133. https://doi.org/10.1016/S0040-1951(97)00133-9

Ji, S., Salisbury, M. H., & Hanmer, S. (1993). Petrofabric, P-wave anisotropy and seismic reflectivity of high-grade tectonites. *Tectonophysics*, *222*(2), 195–226. https://doi.org/10.1016/0040-1951(93)90049-

Ji, S., Shao, T., Michibayashi, K., Long, C., Wang, Q., Kondo, Y., et al. (2013). A new calibration of seismic velocities, anisotropy, fabrics, and elastic moduli of amphibole-rich rocks. *Journal of Geophysical Research: Solid Earth*, *118*, 4699–4728. https://doi.org/10.1002/jgrb.50352

Ji, S., Shao, T., Michibayashi, K., Oya, S., Satsukawa, T., Wang, Q., et al. (2015). Magnitude and symmetry of seismic anisotropy in mica- and amphibole-bearing metamorphic rocks and implications for tectonic interpretation of seismic data from the southeast Tibetan Plateau. *Journal of Geophysical Research: Solid Earth*, *120*, 6404–6430. https://doi.org/10.1002/2015JB012209

Ji, S., Wang, Q., Marcotte, D., Salisbury, M. H., & Xu, Z. (2007). P wave velocities, anisotropy and hysteresis in ultrahigh-pressure metamorphic rocks as a function of confining pressure. *Journal of Geophysical Research*, *112*, B09204. https://doi.org/10.1029/2006JB004867

Ji, S., Wang, Q., & Xia, B. (2003). P-wave velocities of polymineralic rocks: Comparison of theory and experiment and test of elastic mixture rules. *Tectonophysics*, *366*(3–4), 165–185. https://doi.org/10.1016/S0040-1951(03)00094-5

Jones, T., & Nur, A. (1982). Seismic velocity and anisotropy in mylonites and the reflectivity of deep crystal fault zones. *Geology*, *10*(5), 260.

Juhlin, C., Hedin, P., Gee, D. G., Lorenz, H., Kalscheuer, T., & Yan, P. (2016). Seismic imaging in the eastern Scandinavian Caledonides: Siting the 2.5 km deep COSC-2 borehole, central Sweden. *Solid Earth*, *7*(3), 769–787. https://doi.org/10.5194/se-7-769-2016

Kaneshima, S. (1990). Origin of crustal anisotropy: Shear wave splitting studies in Japan. *Journal of Geophysical Research*, *95*(B7), 11121. https://doi.org/10.1029/JB095iB07p11121

Kästner, F., Pierdominici, S., Elger, J., Zappone, A., Kück, J., & Berndt, C. (2020). Correlation of core and downhole seismic velocities in high-pressure metamorphic rocks: A case study for the COSC-1 borehole, Sweden. *Solid Earth*, *11*, 607–626. https://doi.org/10.5194/se-2019-161

Kästner, F., Wenning, Q., Zappone, A., Madonna, C., Morales, L. F. G., Pierdominici, S., et al. (2020). *Seismic properties and mineralogy of core samples from the COSC-1 borehole*. Sweden: GFZ Data Services. https://doi.org/10.5880/GFZ.4.2.2020.009

Kern, H. (1978). The effect of high temperature and high confining pressure on compressional wave velocities in quartz-bearing and quartz-free igneous and metamorphic rocks. *Tectonophysics*, *44*(1–4), 185–203. https://doi.org/10.1016/0040-1951(78)90070-7

Kern, H. (1990). Laboratory seismic measurements: An aid in the interpretation of seismic field data. *Terra Nova*, *2*(6), 617–628. https://doi.org/10.1111/j.1365-3121.1990.tb00127.x

Kern, H., Ivankina, T. I., Nikitin, A. N., Lokajíček, T., & Pros, Z. (2008). The effect of oriented microcracks and crystallographic and shape preferred orientation on bulk elastic anisotropy of a foliated biotite gneiss from Outokumpu. *Tectonophysics*, *457*(3–4), 143–149. https://doi.org/10.1016/j.tecto.2008.06.015

Kern, H., Popp, T., Gorbatsevich, F., Zharikov, A., Lobanov, K. V., & Smirnov, Y. P. (2001). Pressure and temperature dependence of V_P and V_S in rocks from the superdeep well and from surface analogues at Kola and the nature of velocity anisotropy. *Tectonophysics*, *338*(2), 113–134. https://doi.org/10.1016/S0040-1951(01)00128-7

Kern, H., & Wenk, H.-R. (1990). Fabric-related velocity anisotropy and shear wave splitting in rocks from the Santa Rosa Mylonite Zone, California. *Journal of Geophysical Research*, *95*(B7), 11213–11223. https://doi.org/10.1029/JB095IB07P11213

Krauß, F. (2018). *Combination of borehole seismic and downhole logging to investigate the vicinity of the COSC-1 borehole in western Scandinavia*. Freiberg, Germany: TU Bergakademie Freiberg. Retrieved from https://nbn-resolving.org/urn:nbn:de:bsz:105-qucosa2-233719

Ladenberger, A., Be'eri-Shlevin, Y., Claesson, S., Gee, D. G., Majka, J., & Romanova, I. V. (2014). Tectonometamorphic evolution of the Åreskutan Nappe—Caledonian history revealed by SIMS U–Pb zircon geochronology. *Geological Society, London, Special Publications*, *390*(1), 337–368. https://doi.org/10.1144/SP390.10

Leary, P. C., Crampin, S., & McEvilly, T. V. (1990). Seismic fracture anisotropy in the Earth's crust: An overview. *Journal of Geophysical Research*, *95*(B7), 11105–11114. https://doi.org/10.1029/JB095iB07p11105

Lippmann, E., Bücker, C., Huenges, E., Rauen, A., Wienand, J., Wolter, K., & Soffel, H. C. (1989). Rock physical properties: First results of the KTB-field-laboratory. *Scientific Drilling*, *1*(3), 143–149.

Lloyd, G. E., Butler, R. W. H., Casey, M., & Mainprice, D. (2009). Mica, deformation fabrics and the seismic properties of the continental crust. *Earth and Planetary Science Letters*, *288*(1–2), 320–328. https://doi.org/10.1016/j.epsl.2009.09.035

Lorenz, H., Rosberg, J.-E., Juhlin, C., Bjelm, L., Almqvist, B. S. G., Berthet, T., et al. (2015a). COSC-1—Drilling of a subduction-related allochthon in the Palaeozoic Caledonide orogen of Scandinavia. *Scientific Drilling*, *19*, 1–11. https://doi.org/10.5194/sd-19-1-2015

Lorenz, H., Rosberg, J.-E., Juhlin, C., Bjelm, L., Almqvist, B. S. G., Berthet, T., et al. (2015b). *COSC-1 operational report—Operational data sets*. Potsdam, Germany: GFZ Data Services. https://doi.org/10.1594/GFZ.SDDB.ICDP.5054.2015

Mainprice, D., Hielscher, R., & Schaeben, H. (2011). Calculating anisotropic physical properties from texture data using the MTEX open-source package. *Geological Society, London, Special Publications*, *360*(1), 175–192. https://doi.org/10.1144/SP360.10

Mainprice, D., & Humbert, M. (1994). Methods of calculating petrophysical properties from lattice preferred orientation data. *Surveys in Geophysics*, *15*(5), 575–592. https://doi.org/10.1007/BF00690175

Mainprice, D., & Nicolas, A. (1989). Development of shape and lattice preferred orientations: Application to the seismic anisotropy of the lower crust. *Journal of Structural Geology*, *11*(1–2), 175–189. https://doi.org/10.1016/0191-8141(89)90042-4

Mcskimin, H. J., Andreatch, P., & Thurston, R. N. (1965). Third-order elastic coefficients of quartz. *Journal of Applied Physics*, *36*, 988. https://doi.org/10.1063/1.1703099

Meissner, R., Rabbel, W., & Kern, H. (2006). Seismic lamination and anisotropy of the lower continental crust. *Tectonophysics*, *416*(1–2), 81–99. https://doi.org/10.1016/j.tecto.2005.11.013

Morales, L. F. G., Mainprice, D., & Kern, H. (2018). Olivine–antigorite orientation relationships: Microstructures, phase boundary misorientations and the effect of cracks in the seismic properties of serpentinites. *Tectonophysics*, *724–725*, 93–115. https://doi.org/10.1016/j.tecto.2017.12.009

Okaya, D., Rabbel, W., Beilecke, T., & Hasenclever, J. (2004). P wave material anisotropy of a tectono-metamorphic terrane: An active source seismic experiment at the KTB super-deep drill hole, southeast Germany. *Geophysical Research Letters*, *31*, L24620. https://doi.org/10.1029/2004GL020855

Okaya, D., Vel, S. S., Song, W. J., & Johnson, S. E. (2019). Modification of crustal seismic anisotropy by geological structures ("structural geometric anisotropy"). *Geosphere*, *15*(1), 146–170. https://doi.org/10.1130/GES01655.1

Omura, K. (2004). *Anisotropies of electrical conductivities and P wave velocities of cataclasites and mylonites under ambient conditions: Laboratory measurements of Hatagawa* (Report 66). National Research Institute for Earth Science and Disaster Prevention. Retrieved from https://dil-opac.bosai.go.jp/publication/nied_report/PDF/66/66omura.pdf

Prior, D. J., Boyle, A. P., Brenker, F., Cheadle, M. C., Day, A., Lopez, G., et al. (1999). The application of electron backscatter diffraction and orientation contrast imaging in the SEM to textural problems in rocks. *American Mineralogist*, *84*, 1741–1759.

Rabbel, W. (1994). Seismic anisotropy at the continental deep drilling site (Germany). *Tectonophysics*, *232*(1–4), 329–341. https://doi.org/10.1016/0040-1951(94)90094-9

Rabbel, W., Beilecke, T., Bohlen, T., Fischer, D., Frank, A., Hasenclever, J., et al. (2004). Superdeep vertical seismic profiling at the KTB deep drill hole (Germany): Seismic close-up view of a major thrust zone down to 8.5 km depth. *Journal of Geophysical Research*, *109*, B09309. https://doi.org/10.1029/2004JB002975

Rabbel, W., & Mooney, W. D. (1996). Seismic anisotropy of the crystalline crust: What does it tell us? *Terra Nova*, *8*(1), 16–21. https://doi.org/10.1111/j.1365-3121.1996.tb00721.x

Roberts, D., & Gee, D. G. (1985). An introduction to the structure of the Scandinavian Caledonides. In D. G. Gee & B. A. Sturt (Eds.), *The Caledonide Orogen: Scandinavia and related areas* (pp. 55–68). Chichester, UK: Wiley.

Schaeben, H. (1997). A simple standard orientation density function: The hyperspherical de la Vallée Poussin Kernel. *Physica Status Solidi (B)*, *200*(2), 367–376. https://doi.org/10.1002/1521-3951(199704)200:2<367::AID-PSSB367>3.0.CO;2-I

Schoenberg, M., & Muir, F. (1989). A calculus for finely layered anisotropic media. *Geophysics*, *54*(5), 581–589. https://doi.org/10.1190/1.1442685

Siegesmund, S., Kern, H., & Vollbrecht, A. (1991). The effect of oriented microcracks on seismic velocities in an ultramylonite. *Tectonophysics*, *186*(3–4), 241–251. https://doi.org/10.1016/0040-1951(91)90361-U

Siegesmund, S., & Vollbrecht, A. (1991). Complete seismic properties obtained from microcrack fabrics and textures in an amphibolite from the Ivrea zone, Western Alps, Italy. *Tectonophysics*, *199*(1), 13–24. https://doi.org/10.1016/0040-1951(91)90116-A

Simon, H., Buske, S., Hedin, P., Juhlin, C., Krauß, F., & Giese, R. (2019). Anisotropic Kirchhoff pre-stack depth migration at the COSC-1 borehole, central Sweden. *Geophysical Journal International*, *219*(1), 66–79. https://doi.org/10.1093/gji/ggz286

Simon, H., Buske, S., Krauß, F., Giese, R., Hedin, P., & Juhlin, C. (2017). The derivation of an anisotropic velocity model from a combined surface and borehole seismic survey in crystalline environment at the COSC-1 borehole, central Sweden. *Geophysical Journal International*, *210*, 1332–1346. https://doi.org/10.1093/gji/ggx223

Simpson, J., Adam, L., Wijk, K., & Charoensawan, J. (2020). Constraining microfractures in foliated Alpine Fault rocks with laser ultrasonics. *Geophysical Research Letters*, *47*, e2020GL087378. https://doi.org/10.1029/2020GL087378

Strömberg, A. G. B., Karis, L., Zachrisson, E., Sjöstrand, T., & Skogland, R. (1994). Bedrock geological map of Jämtland County (Caledonides), scale 1:200 000. Sveriges Geologiska Undersökning, Ca 53.

Sun, S., Ji, S., Wang, Q., Xu, Z., Salisbury, M., & Long, C. (2012). Seismic velocities and anisotropy of core samples from the Chinese Continental Scientific Drilling borehole in the Sulu UHP terrane, eastern China. *Journal of Geophysical Research*, *117*, B01206. https://doi.org/10.1029/2011JB008672

Thomsen, L. (1986). Weak elastic anisotropy. *Geophysics*, *51*(10), 1954–1966. https://doi.org/10.1190/1.1442051

Vaughan, M. T., & Guggenheim, S. (1986). Elasticity of muscovite and its relationship to crystal structure. *Journal of Geophysical Research*, *91*(B5), 4657. https://doi.org/10.1029/JB091iB05p04657

Vernik, L., Hickman, S., Lockner, D., & Rusanov, M. (1994). Ultrasonic velocities in cores from the Kola superdeep well and the nature of subhorizontal seismic reflections. *Journal of Geophysical Research*, *99*(B12), 24209–24219. https://doi.org/10.1029/94JB01236

Waeselmann, N., Brown, J. M., Angel, R. J., Ross, N., Zhao, J., & Kaminsky, W. (2016). The elastic tensor of monoclinic alkali feldspars. *American Mineralogist*, *101*(5), 1228–1231. https://doi.org/10.2138/am-2016-5583

Weiss, T., Siegesmund, S., Rabbel, W., Bohlen, T., & Pohl, M. (1999). Seismic velocities and anisotropy of the lower continental crust: A review. In *Seismic exploration of the deep continental crust* (pp. 97–122). Basel, Switzerland: Birkhäuser. https://doi.org/10.1007/978-3-0348-8670-3_6

Wenk, H.-R., Vasin, R. N., Kern, H., Matthies, S., Vogel, S. C., & Ivankina, T. I. (2012). Revisiting elastic anisotropy of biotite gneiss from the Outokumpu scientific drill hole based on new texture measurements and texture-based velocity calculations. *Tectonophysics*, *570–571*, 123–134. https://doi.org/10.1016/j.tecto.2012.06.023

Wenning, Q. C., Almqvist, B. S. G., Hedin, P., & Zappone, A. (2016). Seismic anisotropy in mid to lower orogenic crust: Insights from laboratory measurements of V_p and V_s in drill core from central Scandinavian Caledonides. *Tectonophysics*, *692*(A), 14–28. https://doi.org/10.1016/j.tecto.2016.07.002

Wenning, Q. C., Berthet, T., Ask, M., Zappone, A., Rosberg, J.-E., & Almqvist, B. S. G. (2017). Image log analysis of in situ stress orientation, breakout growth, and natural geologic structures to 2.5 km depth in central Scandinavian Caledonides: Results from the COSC-1 borehole. *Journal of Geophysical Research: Solid Earth*, *122*, 3999–4019. https://doi.org/10.1002/2016JB013776

Zang, A., Berckhemer, H., & Lienert, M. (1996). Crack closure pressures inferred from ultrasonic drill-core measurements to 8 km depth in the KTB wells. *Geophysical Journal International*, *124*(3), 657–674. https://doi.org/10.1111/j.1365-246X.1996.tb05631.x